DYNAMICS OF COMPOSITE BEADS IN OPTICAL TWEEZERS AND THEIR APPLICATION TO STUDY OF HIV CELL ENTRY

A Thesis
Presented to
The Academic Faculty

by

Vaclav Beranek

In Partial Fulfillment
of the Requirements for the Degree
Master of Science in Bioengineering

Georgia Institute of Technology

August 2014

DYNAMICS OF COMPOSITE BEADS IN OPTICAL TWEEZERS AND THEIR APPLICATION TO STUDY OF HIV CELL ENTRY

Approved by:

Dr. Cheng Zhu, Advisor
School of Mechanical Engineering
Georgia Institute of Technology

Dr. Evan Evans
School of Biomedical Engineering
Boston University

Dr. Susan N. Thomas
School of Mechanical Engineering
Georgia Institute of Technology

Date Approved: 25 June 2014

ACKNOWLEDGEMENTS

I would like to thank Dr. Evan Evans for his support, mentorship and advice, which were instrumental in completion of this thesis. I would also like to thank Dr. Cheng Zhu, for his supervision and continued support. The passion for science and insight of both of my advisors was a great source of inspiration and learning. My deepest thanks belong to Dr. Igor Kuznetsov for his friendship, advice and support. The software applications for data analysis written by Dr. Kuznetsov were essential to this work, as was his countless advice on all aspects of optical trapping. I am very grateful to all the members of the Zhu Lab for their humor and friendship, which made my stay at the Zhu lab most enjoyable. I would also like to thank my partners in crime from the Bioengineering graduate program: Harrison Norman, Morris Huang, James Wade, Ilya Kolb and William Stoy. My thanks extends also to my father, Pavel Beranek, my mother, Eva Berankova, and my big sister, Vladimira Petrakova, for being the most supportive and loving family. Lastly, I would like to thank Dr. Ruediger Naumann-Etienne, whose foundation has very generously supported me during my stay at Georgia Tech.

Individual chapter contributions: The work in this thesis was shared equally between Vaclav Beranek (VB), Igor R. Kuznetsov (IK), and Evan Evans (EE). In addition to performing the experiments and processing large amounts of data, VB & IK developed the novel optical detection and power control sequence needed to identify and select a specific orientation of the trap microsphere with its appended nanoparticle is either confined local to the top or bottom pole (Chapter 6). EE designed the experiment and developed the energy landscape model describing the equilibrium distribution of

microsphere orientations under broken rotational symmetry as well as the kinetic rates of escape from a present state of microsphere orientation (Chapters 3 and 6). VB implemented and analyzed the Brownian dynamics simulation that modeled rotational symmetry breaking and thermally activated transitions (Chapter 4) and developed the tracking algorithm for the positions of the small bead (Chapter 5). IK developed the post-processing algorithm to correct for optical beam alignment in small bead position data and the algorithm for their analysis (Chapter 6). EE, IK and VB thank Andrew Leung (University of British Columbia) for his help in assembling the optical trap system and in developing chemical methods for particle preparations (Chapter 5). The work has been supported by an NIH subaward to EE from Dr. Cheng Zhu's NIH grant (R01 AI044902-11) and funds from the School of Engineering at Duke University.

TABLE OF CONTENTS

		Page
ACKNOWLEDGEMENTS		iii
LIST OF FIGURES		vii
LIST OF SYMBOLS AND ABBREVIATIONS		viii
SUMMARY		ix
CHAPTER		
1	CHAPTER 1 INTRODUCTION	1
	Structure of the Thesis	1
	Background and Context	3
2	CAHAPTER 2 THEORETICAL DESCRIPTION OF OPTICAL TWEEZERS	6
	Background on Optical Trapping	6
	Forces in Optical Tweezers	7
	Illumination Representation	13
	Electrostatic Approximation	17
3	CHAPTER 3 THEORETICAL ANALYSIS	19
	Beam Waist Estimation	19
	Results of Theoretical Formulation	22
4	CHAPTER 4 BROWNIAN DYNAMICS SIMULATION	31
	Langevin Dynamics	31
	Details of the Simulation Code	33
	Results of the Simulation	34
5	CHAPTER 5 MATERIALS AND METHODS	38
	Optical Tweezers Setup	38

Composite Bead Preparation 39

Large Bead Tracking Algorithm and Spring Constant Calibration 41

Small Bead Tracking Algorithm 43

6 EXPERIMENTAL RESULTS 48

Power Ramp Experiments 48

Quantification of Rotational Confinement 55

7 SUMMARY AND DISCUSSION 60

APPENDIX A: SPRING CONSTANT CALCULATION BASED ON ELECTROSTATIC APPROXIMATION 64

APPENDIX B: SEPARATION OF TIMESCALES FOR TRANSLATIONAL AND ROTATIONAL MOTION OF THE COMPOSITE BEADS 69

REFERENCES 70

LIST OF FIGURES

Page

Figure 1.1: Schematics of a composite bead. 5

Figure 2.1: Gradient force diagram in the ray optics regime. 8

Figure 2.2: Intensity of plane wave scattered by beads of various diameters as a function of scattering angle. 12

Figure 2.3: Comparison of Debye-type integral and Gaussian paraxial representations for a highly convergent beam. 17

Figure 3.1: Beam waist size as a function of the filling ratio α. 21

Figure 3.2: Composite bead trapped in a highly focused beam and the employed coordinate system. 24

Figure 3.3: Intensity at the position of the small bead as a function of polar angle. 25

Figure 3.4: Radial and axial forces acting on the small bead as a function of polar angle. 26

Figure 3.5: Torque exerted by the small bead as a function of the polar angle. 27

Figure 3.6: Energy landscapes of the rotational orientations of the composite bead. 28

Figure 3.7: Top-down symmetry breaking as a function of the bead equilibrium position. 30

Figure 4.1: Brownian dynamics revealing spontaneous symmetry breaking for increasing laser power. 35

Figure 4.2: Normalized histograms of small bead positions as a function of polar angle. 37

Figure 5.1: Schematic of the optical tweezers instrument. 39

Figure 5.2: Overlaid difference interference contrast and fluorescence image of composite beads. 41

Figure 5.3: Tracking algorithm for positions of the large bead. 42

Figure 5.4: Spring constants for varying laser power. 43

Figure 5.5: Traces of large bead position with small bead in “Up” and “Down” states when displaced by movement of the piezostage. 44

Figure 5.6: Image processing algorithm for detection of the small bead position. 45

Figure 5.7: Video of composite bead captured in optical trap.
(S1_Supplementary_Video.avi, 19,540 KB) 47

Figure 5.8: Video of algorithm for tracking of rotation of the composite bead.
(S2_Supplementary_Video.avi, 18,190 KB) 47

Figure 6.1: Power ramp experiment. 50

Figure 6.2: Histogram of intensity metric for detection of "Up" and "Down" states. 51

Figure 6.3: Initial state probabilities for laser power ramp experiment. 54

Figure 6.4: Post-processing of small bead tracking data. 56

Figure 6.5: Mapping of the rotational potential using small bead tracking algorithm. 57

Figure 6.6: Inverse variance of small bead positions as a function of the beam power. 58

Figure A.1: Coordinate transform from cylindrical coordinates to spherical
coordinates. 65

SUMMARY

In this thesis, we report a novel symmetry breaking system in single-beam optical trap. The breaking of symmetry is observed in Brownian dynamics of a linked pair of beads with substantially differing radii (500nm and 100nm). Such composite beads were originally conceived as a manipulation means to study of Brownian interactions between mesoscopic biological agents of the order of 100 – 200 nm (viruses or bacteria) with cell surfaces. During the initial testing of the composite bead system, we discovered that the system displayed thermally activated transitions and energetics of symmetry breaking. This thesis, while making a brief overview of the biological relevance of the composite bead system, focuses primarily on the analysis and experimentation that reveals the complex dynamics observed in the system.

First, we theoretically analyze the origin of the observed symmetry breaking using electromagnetic theory under both Gaussian beam approximation and full Debye-type integral representation. The theory predicts that attachment of a small particle to a trapped microsphere results in creation of a bistable rotational potential with thermally activated transitions. The theoretical results are then verified using optical trapping experiments. We first quantify the top-down symmetry breaking based on measurement of the kinetic transition rates. The rotational potential is then explored using an experiment employing a novel algorithm to track rotational state of the composite bead. The results of the theory and experiments are compared with results of a Brownian dynamics simulation based on Smart Monte Carlo algorithm.

CHAPTER 1

INTRODUCTION

This thesis analyzes a novel symmetry breaking system in single-beam optical trap, which was observed in Brownian dynamics of a linked pair of beads with substantially differing radii (500nm and 100nm). Such system, designated as a composite bead, was originally designed to study Brownian interactions between HIV particles with cell surfaces. During the initial testing of the composite bead system, we discovered that the system displayed thermally activated transitions and energetics of symmetry breaking. This thesis, while making a brief overview of the biological relevance of the composite bead system, focuses primarily on the analysis and experimentation that reveals the complex dynamics observed in the system.

Structure of the Thesis

The work is presented in the following chapters:

Chapter 1, Introduction: Along with overview of the thesis structure, this chapter includes section on motivation behind the experiment from both biological and thermodynamical perspective.

Chapter 2, Theoretical Background: This chapter provides some background on the theory of optical tweezers. In the first part, we overview the main regimes for calculation of forces in optical tweezers: the ray optics regime, the Rayleigh regime and the Mie regime. Subsequently, two theoretical descriptions of illumination which are used in this thesis are introduced: the Gaussian beams and the Debye-type integral description. Lastly, we introduce the electrostatic approximation which is used as a basis to estimate the trapping beam stiffness.

Chapter 3, Theoretical Results: This chapter analyzes the composite bead system using the Rayleigh approximation while comparing two different descriptions of illumination: the full Debye-type integral representation and the Gaussian beam approximation. Based on the theory we draw predictions about the properties of the composite bead system and its behavior.

Chapter 4, Brownian Dynamics: To probe the behavior of composite beads under different experimental conditions we perform Brownian dynamics simulation based on the Smart Monte Carlo algorithm. The chapter starts with introduction of Langevin dynamics, followed by few details on the implementation of the Brownian dynamics simulation. In the last part of this chapter we present the results of the simulation.

Chapter 5, Materials and Methods: In the first two parts of this chapter, we describe the optical tweezers instrument used for the experiments and the protocol for preparation of the composite beads. The third part outlines the method for the instrument calibration and composite bead tracking. In the last section we provide a description of a novel image processing algorithm to track the rotational dynamics of the composite beads.

Chapter 6, Experimental Results and Discussion: This chapter explains the design of the performed experiments to probe the dynamics of the composite beads: the power ramp experiments, the potential mapping experiment and the equilibrium dynamics experiment. The experiments are matched with the results predicted by the Brownian dynamics simulation.

Chapter 7, Summary and Discussion: Here we briefly summarize and discuss the major findings in the thesis and envision future research directions and applications of composite beads.

Appendix A: The first appendix consist of the derivation of theoretical formulas – based on the electrostatic approximation – to calculate the optical trap spring constants for the composite bead.

Appendix B: In this appendix we provide the calculation to verify the separation of timescales between the translational and rotational motion of the composite beads.

Background and Context

This chapter follows by presenting some of the background on both biological and thermodynamical applications of optical trapping and explains the motivation behind the current work.

Motivation from Biological Perspective

Over the last few decades, optical tweezes provided crucial insights to diverse biological phenomena on the size scales spanning from individual molecules to whole cells. This powerful technique, which allows researchers to precisely manipulate microscopic objects and measure sub-piconewton forces, has been successfully used to study cellular machines such as motor proteins, mechanoenzymes, receptor ligand interactions[1, 2] as well as mechanics on the cellular level [3].

The biological objects of interest in this work are viruses and small bacteria, which generally fall into the size interval of ~ 100 – 200 nm. While first trapping experiments with bacteria and virus particles have been demonstrated already in 1987 [4], it still remains difficult to conduct quantitative experiments with biological objects of these dimensions. Such objects are too small for simple direct manipulation and tracking with optical tweezers (they are below the diffraction limit), but are substantially larger than the most commonly studied proteins.

When working with purified proteins, the optical tweezers experiments generally employ glass or polystyrene microsphere handle with the proteins of interest immobilized on its surface. The well-defined geometry and material properties of the microsphere handle in addition to its relatively large size allow researchers to calibrate and measure forces exerted on the surface coated proteins. The effects of the attached proteins on the

microsphere handle are generally negligible due to both small size of the immobilized proteins and their homogeneous distribution. On the other hand, immobilizing larger objects, such as virus particles with diameter > 100 nm, on the microsphere handle may already significantly affect the probe behavior (Figure 1.1A). Information about the dynamics of such composite beads provides relevant insights for studies of biological objects that remain largely unexplored by the optical tweezing community

Motivation from Physical Perspective

Besides biological applications, optical tweezers have been used to study various physical phenomena, such as activated escape from a metastable states [5], stochastic resonance [6] and many studies in colloidal physics [7]. Recently, optical tweezers have been used to study the energetics of symmetry breaking [8], and provide experimental verification of link between information and thermodynamics by providing a model for one-bit memory erasure [9] or construction of information-to-heat engine [10]. Further, specifically created optical landscapes with optical tweezers can provide insight into various atomic level mechanisms [11].

As will be shown in the following chapters, the composite beads are a very simple dynamical system that exhibits spontaneous symmetry breaking which can be easily controlled by the trapping beam power. A particle trapped in optical tweezers is a subject to thermal excitations from the environment, which result in random force and torque input on the microsphere (Figure 1.1, gray arrows). The trapping beam creates a harmonic potential well, confining the translational motion of the particle to a small volume around the center of the trap. However, there is no torque transfer from the beam to the bead in optical traps using plane polarized laser beams and the bead is therefore free to rotate in the optical tweezers, subject only to rotational friction.

As will be shown in the following chapters, the attachment of a small particle (Fig. 1.1B) results in a breaking of the rotational symmetry, confining the rotational states

of the composite bead into two bistable orientations between which – under specific experimental conditions – thermally activated transitions can be observed.

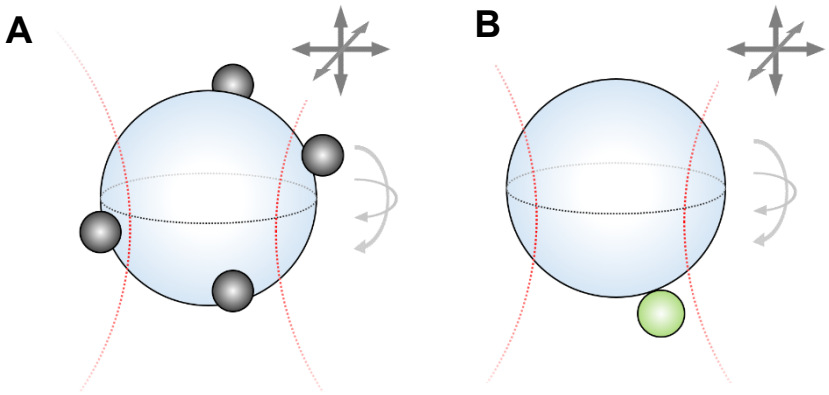

Figure 1.1. Schematic of a composite beads. (A) 1 µm borosilicate bead with four attached VLPs with 140 nm diameter. (B) A simplified model made of a 1 µm borosilicate bead and a single 200 nm polystyrene bead. The large borosilicate beads experience forces exerted by the optical trap as well as the thermal excitations from the environment in all three spatial directions (grey arrows).

CHAPTER 2

THEORETICAL DESCRIPTION OF OPTICAL TWEEZERS

This chapter consists of theoretical description of forces and illumination in optical tweezers. In the first part, the development of optical trapping is briefly discussed and the three basic regimes of theoretical description – ray optics regime, Rayleigh regime, and Lorenz-Mie theory – are overviewed. These are followed by a review of two models of illumination in optical tweezers: Gaussian beams and Debye-type integral representation. We designate the last section to a brief introduction of the electrostatic approximation.

Background on Optical Trapping

The idea that light could exert mechanical forces on particles was conceived already in the 17th century by Johannes Kepler when observing tails of comets [12]. More than two and a half century later, James Clerk Maxwell introduced this idea in his theory of electromagnetic field [13]. According to Maxwell, electromagnetic wave carries a momentum which can be transferred to matter through absorption, reflection, or refraction and the force exerted on the surface is proportional to the rate of change in the wave's momentum.

While generally very weak, forces exerted by a light beam can be used to manipulate small particles of matter. This was first demonstrated by Arthur Ashkin in 1970, when he observed that after focusing a beam of laser light on latex spheres suspended in water, the spheres were "simultaneously drawn in to the beam axis and accelerated in the direction of the light" [14]. This observation led Ashkin to conclude and later theoretically describe [15] that the forces in optical trap can be decomposed into radiation pressure force, acting in the direction of the beam, and gradient forces, pulling

the particle into the center of the focused beam. The technique of using light to precisely manipulate small particles called "optical tweezers" has since then helped dramatically advance our understanding of mechanics, dynamics, and kinetics of many biological systems and molecules such as motor proteins, nucleic acids, and many others [16].

Forces in Optical Tweezers

The trapping forces in optical tweezers can be viewed as a result of a competition between radiation pressure, acting on the particle along the axis of beam propagation, and gradient forces, pulling the particle along the gradient towards the highest intensity. However, both of these forces are a result of the same underlying physical phenomena. While particles of arbitrary geometry can be manipulated by optical tweezers, the discussion here is limited to a homogeneous dielectric sphere, which is the particle of choice for most of experiments.

The theoretical description of optical traps can be significantly simplified under one of two conditions: 1) size of the trapped particle is much larger than the wavelength of light λ – the so called ray optics regime or 2) the size of trapped particle is much smaller than the wavelength λ – the Rayleigh regime. The complete theory of optical tweezers, which can be used for particles of arbitrary size is based on Lorenz-Mie theory.

Ray Optics Regime

In the ray optics regime, the trapped particle can be viewed as a positive lens and the trapping beam is represented as a bundle of rays, each carrying an appropriate intensity, direction, and polarization. This idea was first introduced and quantitatively analyzed by Arthur Ashkin [17, 18]. Given that the momentum in the system is conserved, one can, through of Newton's second law, determine the forces on the trapped particle by looking at the changes in momentum flux of the trapping beam. A qualitative image of this situation is shown in Fig. 1.1. If the particle is positioned above the focus of

the beam (Fig. 2.1B), the divergence of the incoming rays is increased. The lost momentum in the axial direction is transferred to the particle, resulting in a force pointing downwards towards the focal point. A particle positioned bellow the focus decreases the divergence of incoming rays (Fig. 2.1A), resulting in restoring forces pointing in the opposite direction. Lastly, in the case of transverse displacement (Fig. 2.1C), the beam gains transverse momentum, giving rise to restoring force in the lateral direction.

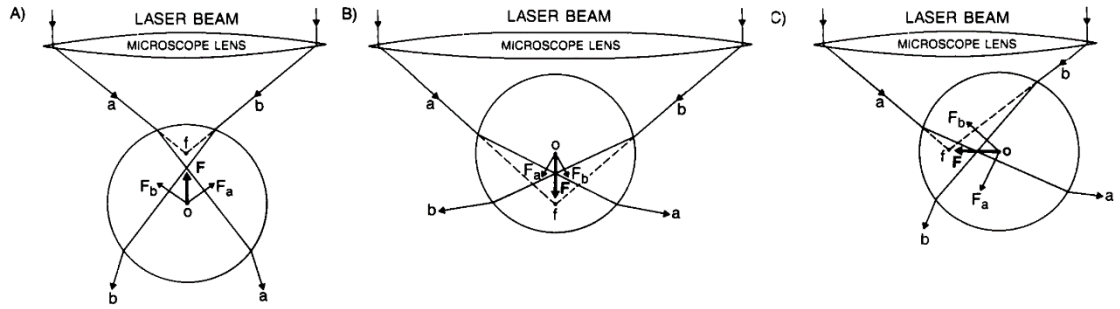

Figure 2.1. Gradient force diagram in the ray optics regime. The refraction of a pair of trapping beams a and b gives rise to forces F_a and F_b acting on the trapped particle. The sum of these forces F acts as a restoring axial (A and B) or transverse (C) force, pointing to the focal point of the trap (modified from [19]).

To calculate the momentum flux of a ray of light, we consider a momentum flux of a section of a plane wave given by $p = nP/c$, where n is the refractive index of the medium, P is the power and c is the speed of light. A plane wave can then be represented as a bundle of parallel rays, while focused beam can be characterized as a bundle of rays converging to a single point.

The force due to radiation pressure is represented by partial reflection of the incoming beams. A detailed quantitative analysis of the ray optics regime of the optical trap for spherical particles is developed in [18].

The limitation of the ray optics analysis is given by the assumption $R \gg \lambda$. Generally, at least 5-fold difference between R and λ is required for ray optics regime to provide precise quantitative predictions [1]. This assumption allows one to neglect the complex interaction of the particle with the electromagnetic field as well as the inaccurate description of highly focused beams by the means of geometrical optics.

Rayleigh Regime

If the trapped particle is comparable or smaller than the wavelength of the trapping light, the diffraction effects become important. Given that $R \ll \lambda$ one can assume that the field acting on the particle will be uniform and approximate the trapped particle as a single dipole.

The electromagnetic field acts on a sphere of radius a and induces a dipole moment given by [20, 21]:

$$p(\boldsymbol{r}, t) = 4\pi\varepsilon_2 a^3 \left(\frac{\varepsilon_1 - \varepsilon_2}{\varepsilon_1 + 2\varepsilon_2}\right) E(\boldsymbol{r}, t) = 4\pi n_2^2 \varepsilon_0 a^3 \left(\frac{m^2 - 1}{m^2 + 2}\right) E(\boldsymbol{r}, t) \qquad (2.1)$$

where ε_1 and ε_2 represent the dielectric constants of the particle and the surrounding medium, respectively, and m is the relative refractive index of the particle and the surrounding medium $m = n_1/n_2$. To obtain the right side of the equation (2.1), we use the relations $c/n_1 = (\varepsilon_1 \varepsilon_0 \mu_0)^{1/2}$ for the non-magnetic sphere and $\varepsilon_2 = \varepsilon_0 n_2^2$ and $\mu_2 = \mu_0$ for the non-conducting, non-magnetic surrounding medium where μ_2 is the magnetic permeability of the surrounding medium.

The induced dipole changes in time, following the time oscillations of the electromagnetic field, and therefore acts as a source of secondary or scattered waves. Since the energy re-radiated by the particle is removed from the incident beam and has total momentum flux of zero, momentum is subtracted from the incident beam resulting in a scattering force given by [16, 22]:

$$F_{\mathrm{scat}}(\boldsymbol{r}) = n_2 \frac{C_{\mathrm{scat}}\langle S(\boldsymbol{r},t)\rangle_{\mathrm{T}}}{c} = z\left(\frac{n_2}{c}\right) C_{\mathrm{scat}} I(\boldsymbol{r}) \tag{2.2}$$

where z is the propagation direction of the incident beam and $\langle S(\boldsymbol{r},t)\rangle_{\mathrm{T}}$ is the time-averaged Poynting vector. C_{scat} is the scattering cross section given by [16, 21]:

$$C_{\mathrm{scat}} = \frac{8}{3}\pi(ka)^4 a^2 \left(\frac{m^2-1}{m^2+2}\right)^2. \tag{2.3}$$

Here k is the wavenumber in the surrounding medium $k = 2\pi/\lambda$. In the Rayleigh regime, the scattering force is an analog to the radiation pressure in the geometrical optics analysis, given that it is proportional to the energy flux of the incident beam and acts in a direction of the beam propagation.

Second component – the gradient force – arises due to the Lorentz force acting on the induced dipole. The dipole in electromagnetic field has a potential energy proportional to $p(\boldsymbol{r},t)\cdot E(\boldsymbol{r},t)$ [20] and the force extended on the dipole is equal to the negative gradient of the potential energy. Using the relation (2.1) for the induced dipole and $\nabla\times E = 0$ as a consequence of Maxwell equations, one obtains following relation for the instantaneous gradient [22]:

$$F_{\mathrm{grad}}(\boldsymbol{r},t) = 4\pi n_2^2 \varepsilon_0 a^3 \left(\frac{m^2-1}{m^2+2}\right)\frac{1}{2}\nabla E^2(\boldsymbol{r},t) \tag{2.4}$$

and the time averaged relation:

$$F_{\mathrm{grad}}(\boldsymbol{r}) = \langle F_{\mathrm{grad}}(\boldsymbol{r},t)\rangle_{\mathrm{T}} = \frac{2\pi n_2 a^3}{c}\left(\frac{m^2-1}{m^2+2}\right)\nabla I(\boldsymbol{r}) \tag{2.5}$$

It is clear that to construct a stable single-beam optical trap, the gradient force must be greater than the scattering force to prevent the escape of the particle. This is

usually achieved by using a high NA objectives, which increase the gradient forces in all directions.

Lorenz-Mie Theory

In practice, the size range of the spheres used in experiments usually falls between the ray optics and Rayleigh regimes, making the theoretical description more complicated. The general approach is to calculate the electromagnetic field by solving the Maxwell for the field outside of the trapped particle and then integrate the Maxwell stress tensor over its surface. Because the particles used in most experiments are homogeneous spheres, one can take advantage of the Lorenz-Mie theory [23, 24], which provides analytical solution of the Maxwell equations for an arbitrarily sized homogeneous sphere in a plane wave. The mathematical treatment of the Lorenz-Mie theory is outside of the scope of this work. Instead, some results of the theory are presented to illustrate the transition from Rayleigh regime to the Mie regime. In Figure 2.1, intensity scattered by a homogeneous sphere is plotted as a function of the scattering angle for spheres of various sizes. The parameters used for the calculations were selected to match the conditions of the experiments in this work.

For bead diameter 0.1 μm on can see that the illuminating plane wave gets scattered into every direction equally, a situation corresponding to the Rayleigh regime. It is interesting to note that in the Rayleigh regime, the scattering force (along the beam axis) scales with the sixth power of the bead radius (Eq. 2.2 and 2.3), while the gradient force scales only with the third power of the bead radius (Eq. 2.5). Increasing the bead size should therefore lead to the ejection of the bead from the trap, as the scattering force eventually overcomes the gradient force. From experiments we see that this is not the case because as we gradually increase the bead size into the Mie regime, it starts to scatter the light from the incoming plane wave mostly forward, as shown in Fig. 2.2. Due

to complex interference of the electromagnetic waves inside the sphere, the scattering quickly becomes very complex.

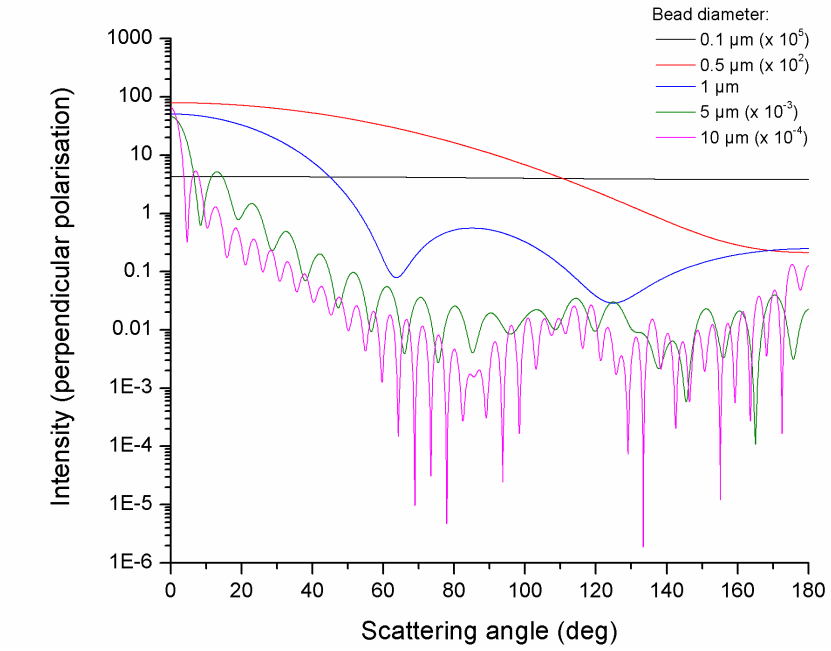

Figure 2.2. Intensity of plane wave scattered by beads of various diameters as a function of scattering angle. The plot shows the transition from homogeneous scattering for very small Rayleigh particles (black line) to the complex Mie scattering produced by medium and large sized beads. The parameters used for the calculation were: $\lambda = 1064$ nm, $a = 0.5$ µm, $n_2(\text{sphere}) = 1.55$ and $n_1(\text{medium}) = 1.33$. The intensities were calculated using the MiePlot program developed by Philip Laven [25].

While the Lorenz-Mie theory is mathematically complex, the solutions are well-known and a number of numerical solutions are available. The main complication of this approach lies in the non-planar, highly focused illumination in the optical trap, a subject of the next chapter. A detailed treatment of the Lorenz-Mie theory is available in [26].

Illumination Representation

Number of approaches have been developed to describe the non-planar, highly focused illumination in optical traps, falling into two main categories: corrections of the Gaussian beam description [27] and Debye-type integral representation of highly focused beams [28].

Gaussian Beams

The Gaussian beams represent an electromagnetic beams whose electric field as well as intensity have a Gaussian profile in the transverse plane and are widely used in the theory of lasers. Mathematically, Gaussian beam is the lowest order solution of the paraxial wave equation

$$\frac{\partial^2 E}{\partial x^2} + \frac{\partial^2 E}{\partial y^2} - 2ik = 0, \tag{2.6}$$

where $k = 2\pi/\lambda$ is the wave number in the given medium. The paraxial wave equation assumes that the wave amplitude changes caused by diffraction effects vary only slowly in the direction of beam propagation compared to the optical wavelength and the transverse variations due to the finite width of the beam. This assumption results in some limitations of the applicability of Gaussian beams especially for the case of highly focused beams. The lowest order solution of the equation (2.6) gives rise to the formula for the complex electric field [29]:

$$E(\boldsymbol{r}) = E_0 \frac{w_0}{w(z)} \exp\left(\frac{-(x^2+y^2)}{w(z)} - ikz - ik\frac{x^2+y^2}{2R(z)} + i\psi(z)\right) \tag{2.7}$$

where $\boldsymbol{r}(x, y, z)$ specifies the position in the beam, E_0 is the amplitude at the center of the beam, $w(z)$ is the radius at which the amplitude decreases to $1/e$ of its center value, w_0 is the waist size at $z = 0$, $R(z)$ is the radius of curvature of the propagating wavefront,

and $\psi(z)$ is the Gouy phase shift resulting from the beam passing through the focal region. In the theory of optical tweezers, one is generally more interested in the intensity of the electric field, which is related to the field amplitude by relation $I(\boldsymbol{r}) = |E(\boldsymbol{r})|^2/2\eta$, where η is the characteristic impedance of the given medium. The resulting intensity distribution of the Gaussian beam is then

$$I(\boldsymbol{r}) = I_0 \left(\frac{w_0}{w(z)}\right)^2 \exp\left(\frac{-2(x^2+y^2)}{w^2(z)}\right), \tag{2.8}$$

where I_0 is the intensity at the center of the beam. When propagating in free space, the Gaussian beam behavior can be described by only two parameters – the waist size w_0 and the wavelength in the given medium λ. The beam width is given by

$$w(z) = w_0 \sqrt{1 + \left(\frac{z}{z_R}\right)^2}, \tag{2.9}$$

where z_R denotes the so-called Rayleigh range equal to $z_R = \pi w_0^2/\lambda$. At this distance, the beam radius increases by the factor of $\sqrt{2}$. The radius of curvature develops according to the relation

$$R(z) = z\left[1 + \left(\frac{z_R}{z}\right)^2\right]. \tag{2.10}$$

As a solution to the paraxial Helmholtz equation, the Gaussian beam representation is accurate as long as most of its plane wave components travel under angles less than $\theta < 30°$ [29]. This somewhat limits the use of Gaussian beams to an investigation of systems with low NA. Despite these limitations, analysis of such systems provides useful insights into the physics of optical tweezers. Detailed investigations of trapping forces in Gaussian beams were carried out by Ashkin et al. [15] in the ray optics regime and by Harada and Asakura [22] in the Rayleigh regime.

For the case of illumination by high NA objective, which is the case for majority of the single-beam optical traps, corrections to the Gaussian beams become useful. Most notable theoretical development using the corrected paraxial Gaussian beams was done by Gouesbet *et al*. [30, 31] in the so-called generalized Lorenz-Mie theory (GLMT). In their initial work, Gouesbet *et al*. used the paraxial Gaussian TEM_{00} model with fifth-order corrections originally derived by Davis [32] and modified and extended by Barton and Alexander [33]. Later in the development of the GLMT, localized approximations to the beam-shape coefficients were introduced [34]. The development of GLMT is summarized in [35]. Different approach employing the Lorenz-Mie theory and paraxial Gaussian beams was developed by Nieminen et al. [36] through use of an overdetermined point-matching scheme.

Debye-type Integral Representation

A proper wave description of a highly focused beam based on the exact wave equation was developed by Richards and Wolf in 1959 [28] and is given by a Debye-type integral, which represents the laser beam as a series of converging plane waves. The Richards-Wolf representation was adopted in theoretical treatment of Rohrbach et al. [37] for sub-wavelength particles in the Rayleigh regime. An agreement with experimental results was later shown by the same research group in [38].

The first rigorous description using the full Lorenz-Mie theory in combination with Richards-Wolf representation was developed by Neto et al. [39]. Initially, the trapping forces along the trap axis were calculated, followed by an expansion to transverse trapping forces by Mazolli et al.[40]. Most recently, spherical aberrations arising at the cover glass-water interface were incorporated into this model by Viana et al. [41] in the so-called Mie-Debye-spherical aberration (MDSA) theory.

To illustrate the Richards-Wolf representation, we follow the approach of Neto et al. [39]. The incident beam *before* the objective is described as Gaussian:

$$E_{\text{in}}(\mathbf{r}, z) = E_0 e^{ikz} e^{-\frac{\rho^2}{w_e^2}} (\hat{\boldsymbol{x}} \pm i\hat{\boldsymbol{y}}) e^{-i\omega t} \tag{2.11}$$

where $k = |\boldsymbol{k}(\theta, \phi)| = n_1 \omega / c$, E_0 is the amplitude at the beam axis, ρ is the distance to the beam axis, and w_e is the waist of the beam. Omitting the time factor $e^{-i\omega t}$, the Debye-type integral representation of the focused beam beyond the objective is

$$E_{\text{in}}(\mathbf{r}) = E_0 \int_0^{2\pi} \mathrm{d}\phi \int_0^{\theta_0} \mathrm{d}\theta \sin\theta \sqrt{\cos\theta}\, e^{-\gamma^2 \sin^2\theta} e^{i\boldsymbol{k}\cdot(\boldsymbol{r}+\boldsymbol{R})} \hat{\epsilon}(\theta, \phi) \tag{2.12}$$

where $\hat{\boldsymbol{\epsilon}}(\theta, \phi) = \hat{\boldsymbol{x}}' + i\hat{\boldsymbol{y}}'$, with the unit vectors $\hat{\boldsymbol{x}}'$and $\hat{\boldsymbol{y}}'$ are calculated by rotation of $\hat{\boldsymbol{x}}$ and $\hat{\boldsymbol{y}}$ with Euler angles $(\phi, \theta, -\phi)$. The Abbe sine condition $\rho = f \sin\theta$ (where f is the focal length) gives rise to the factor $\sqrt{\cos\theta}$ and defines $\gamma = f / w_e$ as the ratio of the objective focal length to the beam waist. It is apparent that the equation (2.12) represents a superposition of a series of plane waves converging to a focal point $\boldsymbol{r} = -\boldsymbol{R}$, as initially derived by Richards and Wolf. The scattered field can then be established from the Mie theory using an integral transform [41].

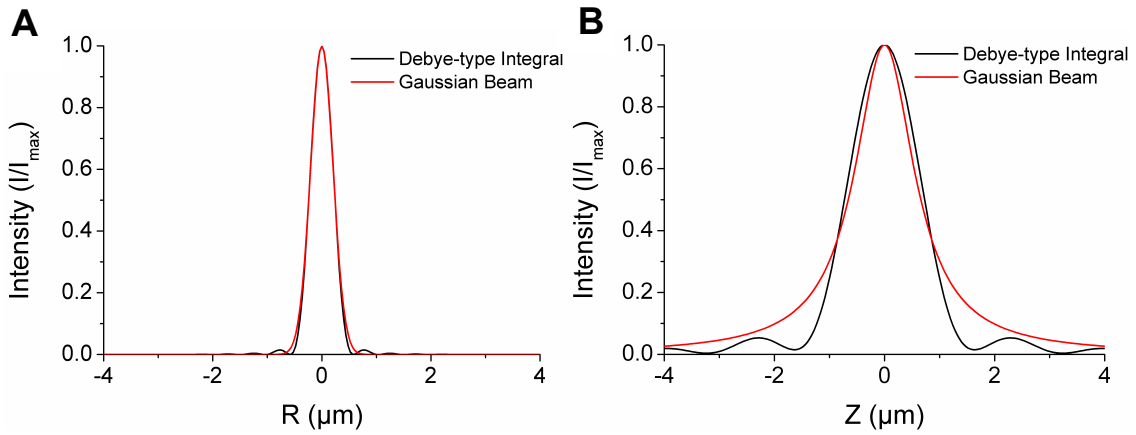

Figure 2.3. Comparison of Debye-type integral (black) and Gaussian paraxial (red) representations for a highly convergent beams. The parameters used are NA = 1.3, filling ratio $\alpha = 1$ [42], $\lambda = 0.806$ μm with the focal length determined from the ratio of manufacturer's tube length and the magnification of the objective. The width of the Gaussian beam w_0 is determined from matching the FWHM of the Gaussian beam and the Richards-Wolf beam in the transversal plane. For a detailed account of calculation of the Debye-type representation and discussion of the filling ratio α see Chapter 3. (A) Intensity profile in the focal plane. (B) Intensity profile along the beam axis showing a slight discrepancy between the Gaussian and Debye-type integral beams for the high NA objective.

Electrostatic Approximation

For particles in the intermediate regime in highly focused beams, Tlusty et al. [43] introduced a simplified approach, based on the assumption that in highly focused electric fields the main contribution comes from the gradient force rather than the scattering force. In their derivation Tlusty et al. calculate the Maxwell stress tensor on the surface of the bead and express the force acting on the sphere as a change in the surface interaction with respect to changing particle coordinates.

A complimentary approach for a Gaussian standing wave from Zemanek et al. [44] is based on the notion that the total energy of the electromagnetic field W is changed by introduction of a dielectric object. This change is equal to the difference between the initial field and the field perturbed by the inserted object and can be expressed as an integral over the whole space of the field V

$$\Delta W = -\frac{1}{2}\int_V (\mathbf{ED} - \mathbf{E_0 D_0} + \mathbf{HB} - \mathbf{H_0 B_0})\mathrm{d}V \tag{2.13}$$

where **E** and **D** are the electric field vector and electric displacement, **H** and **B** are the magnetic field vector and magnetic induction, and the subscript "$_\mathbf{0}$" designates the respective fields before the insertion of the dielectric object. Zemanek et al. [44] have shown that for non-magnetic dielectrics the time-averaged energy difference values can be rewritten as

$$\langle \Delta W(\boldsymbol{r}, t)\rangle_T = -\frac{1}{2}\epsilon_2 \alpha \int_{V_1} \langle \mathbf{E}(\boldsymbol{r}, t)\mathbf{E_0}(\mathbf{r}, t)\rangle_T \mathrm{d}V \tag{2.14}$$

where $\alpha = \frac{\epsilon_1}{\epsilon_2} - 1$ represents the relative difference in the permittivity of the particle $\epsilon_1$and the surrounding medium ϵ_2, and the integral is carried over the volume of the particle V_1. For particles which are only weakly polarizable (in other words, the refractive indices of the particle n_1 and the surrounding medium n_2 are comparable), one can use the unperturbed electric field $\mathbf{E_0}$ to approximate the field perturbed by the presence of the particle **E**. Assuming mainly transverse polarization of the beam, the resulting formula for the field energy change is

$$\Delta W(\boldsymbol{r}) = -\frac{\alpha}{2}\frac{n_2}{c}\int_{V_1} I_0(\mathbf{r})\mathrm{d}V \tag{2.15}$$

The optical force acting on the particle is equivalent to the gradient of the energy change with respect to the particle position $\boldsymbol{r}$. Using the divergence theorem, one can derive the final formula for the force

$$F(\mathbf{r}) \equiv -\nabla\langle \Delta W(\boldsymbol{r}, t)\rangle_T = -\frac{\alpha}{2}\frac{n_2}{c}\int_{V_1} \nabla I_0(\mathbf{r})\mathrm{d}V = -\frac{\alpha}{2}\frac{n_2}{c}\int_{S_1} \mathbf{n} I_0(\mathbf{r})\mathrm{d}S \tag{2.16}$$

CHAPTER 3

THEORETICAL ANALYSIS

In this chapter, we present a theoretical analysis of the forces acting on composite beads trapped in optical tweezers. In the first part, we estimate the beam waist using numerical integration of the Debye-type representation of highly convergent beams. Then we calculate the field intensities that are experienced by the small bead at different positions along the surface of the large bead from which we estimate the forces acting on the small sphere. At the end of this chapter, we present the resulting potential energy landscapes for different rotational states of the composite bead and investigate their properties as a function of the composite bead equilibrium position. Throughout this chapter, we compare results obtained using full Debye-type integral representation and Gaussian approximation.

Beam Waist Estimation

To calculate the forces acting on a composite bead we first need to establish the waist size of the trapping beam. As introduced in Chapter 2, the Debye-type integral representation doesn't require a previous knowledge of the beam waist at the focal plane but rather uses the width of the beam entering the objective w_e. For the case of Gaussian beams, the beam width at the focal plane w_0 is one of the defining parameters and is therefore essential for our calculations. Since we were unable to measure the waist of the beam entering the objective, we investigated the beam width at the focal plane as a function of the beam width of the beam entering the objective.

Following Mahamdeh et al. [42], we define a filling factor

$$\alpha = \frac{2w_e}{D_{\mathrm{NA}}} \tag{3.1}$$

where w_e is the width at which the entering beam intensity decreases to e^{-2} and D_{NA} is the diameter of the so-called exit pupil of the microscope objective. This diameter is not based on the visible stop at the back of the objective but rather on the Abbe's sine condition and thereby is independent of the objective manufacturer (Fig. 3.1, inset). Because the objective satisfies the Abbe's sine condition, the radial distance of the beam converging from angle θ is given by $r = nf \sin\theta$, where n is the refractive index of the lens. To calculate the exit pupil diameter, we use the definition of numerical aperture $\mathrm{NA} = \mathrm{n}\sin\theta$ to finally obtain $D_{\mathrm{NA}} = 2f\mathrm{NA}$, where f is the focal length of the objective (Figure 3.1 inset). To find the focal length, we divide the manufacture's tube length by the magnification of the objective ($f = 164\ \mathrm{mm}/100 = 1.64\ \mathrm{mm}$).

Now we have all the necessary parameters to investigate the beam width at the focal plane based on the Debye-type integral representation, varying only the filling ratio α. Using the parameters of our experimental setup ($\mathrm{NA} = 1.3$, $\lambda_0 = 1.064$ μm), we numerically integrate the equation 2.12 for on-axis values of the trapping beam (Fig. 2.3 black). The values of α are varied from 0.2 to 3, which correspond to the entering beam width w_e of 0.43 mm to 6.3 mm. In the last step, we match each the radial profile of the highly focused laser beam to a Gaussian beam with equivalent FWHM (Fig. 2.3). In Fig. 3.1 are plotted the fitted Gaussian beam widths w_0 that match corresponding filling ratio (beam intensity for value $\alpha = 1$ are shown in Fig. 2.3).

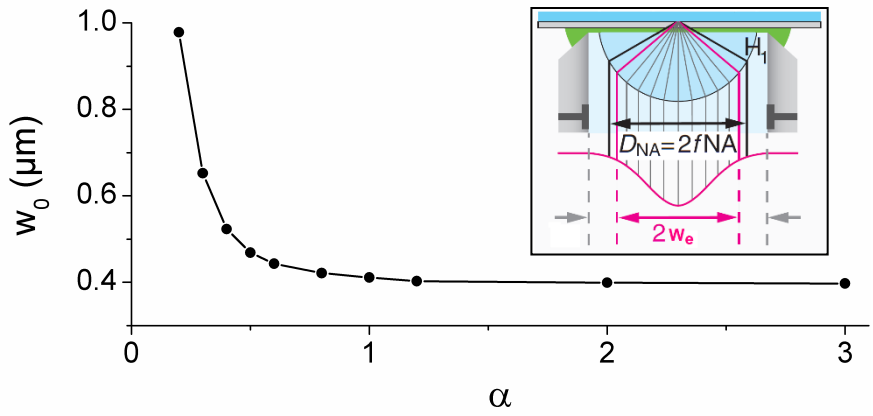

Figure 3.1. Beam waist size as a function of the filling ratio α. The beam waist size represents a Gaussian beam that was matched to a beam calculated by numerical integration of the Debye-type integral (we match the FWHM values of the two beams). Overfilling the objective leads to tighter focusing of the beam but is ultimately limited by diffraction and the numerical aperture of the objective. The inset (adapted from [42]) shows the defining metrics of the filling ratio: the beam width of the beam entering the objective w_e and the exit pupil diameter D_{NA}.

Fig 3.1 illustrates very well the effect of overfilling ($\alpha < 1$) and underfilling ($\alpha < 1$) of the microscope objective. Under-filling the objective leads to lower "effective NA" of the system (maximum angle components have very low amplitude). In such cases, the Gaussian beam approximation will become more accurate as α decreases. Conversely, overfilling the objective leads to tighter focusing (objective is more uniformly filled) and therefore a higher discrepancy between Gaussian beam and the exact Debye-type integral will be present. It is interesting to note that there is no inherent limit for a Gaussian beam width and w_0 can theoretically be made arbitrarily small (which is, of course, in violation of the diffraction limit). In contrast, the Debye-type integral representation does not allow arbitrarily small focal spot, as apparent from the asymptotic nature of the curve in Fig. 3.1 for high values of α.

In our calculations, we use the value of $\alpha = 1$, which corresponds to a Gaussian beam waist $w_0 = 411$ nm. We choose this value because we are fairly confident that we do not underfill the microscope objective and the beam waist doesn't change significantly

for higher values of α. A supportive evidence for overfilling of the microscope objective is shown in Chapter 6, where we estimate that the laser power at the focus is less than 1/5 of the input beam. Such significant drop in laser power is unlikely only due to transmittance of the objective (~ 70% at $\lambda = 1.064$ μm, according to the manufacturer's specifications) and is therefore probably caused by overfilling of the objective.

Results of Theoretical Formulation

With an estimate for the beam width, we can now analyze the forces and torques that act on the composite bead. In the process, we compare the two beam representations: the Debye-type integral representation and the Gaussian beam approximation. Since the beads trapped in optical tweezers generally stay slightly behind the center of the trapping beam [40], I analyzed two equilibrium positions of the large bead in this chapter: 1) in the center of the trapping beam (Fig. 5.1A, solid line) and 2) 143 nm behind the focal point of the trapping beam (Fig. 5.1A dashed line). This equilibrium shift is on the order of the geometrical optics prediction $z_{eq}/a = 0.286$ [40]. However, it is generally quite difficult to estimate from theory the equilibrium position of a trapped microsphere. As will be shown at the end of the chapter and in Chapter 6, the composite bead system allows us to experimentally measure this position.

To get better intuition of the effect of forces acting on the composite bead, we separate them into forces acting on the large bead and forces acting on the small bead. Due to the very large ratio of volumes between the large and the small bead (the diameters used in this chapter are 600 nm and 100 nm for the large and the small bead, respectively, which amount to volume ratio ~ 125) we consider the large bead to be the dominant factor in the translational motion of the composite bead. We therefore neglect the contribution of the small bead to the translational motion of the composite bead and only consider its effect on the rotation of the system. For the purpose of the translational motion, we simply approximate the optical tweezers as a harmonic potential well. To

calculate the spring constants from the trapping beam waist and beam power we use theoretical formulas based on the electrostatic approximation, which are presented in Appendix A along with their derivation.

The rest of this chapter analyzes the forces acting on the small bead and their effect on the rotational motion. To analyze the forces on the small bead, we make two assumptions: 1) the bead is stationary at the equilibrium and 2) the beam outside of the large sphere is not altered significantly by its presence. Both of these assumptions are justified by the separation of timescales on which the translational and the rotational motion occur, which is shown to be over 10^2 even for extremely low trap stiffness in Appendix B. Under the first assumption, the results presented here for a composite bead standing stationary at the center of the trap represent a "mean intensity" or "mean force", etc. that the small bead feels over short time period, as the whole composite bead quickly fluctuates around equilibrium. The second assumption is based on the basic principle of optical trap – the transfer of momentum from the trapping beam to the trapped sphere. When the bead is positioned outside the equilibrium, it changes the momentum of the trapping beam by changing its divergence (force in axial direction) or direction (force in radial direction) (see Fig. 2.1). However, when the bead is in equilibrium, both the divergence and the direction of the beam stays exactly the same and therefore the same argument using separation of timescales applies.

The calculations were performed using Gaussian beam width $w_0 = 411$ nm and composite bead size matching our experimental setup (large bead radius = 0.6 μm, small bead radius = 0.1 μm), considering two glass beads of refractive index $n_2 = 1.52$. To gain better understanding of the effect that the small bead has on the overall dynamics, we first plot the intensity at the position of the small bead at various positions along the polar angle θ (see figure 3.2B). Because of the rotational symmetry of the problem, there is no dependency on the angle φ.

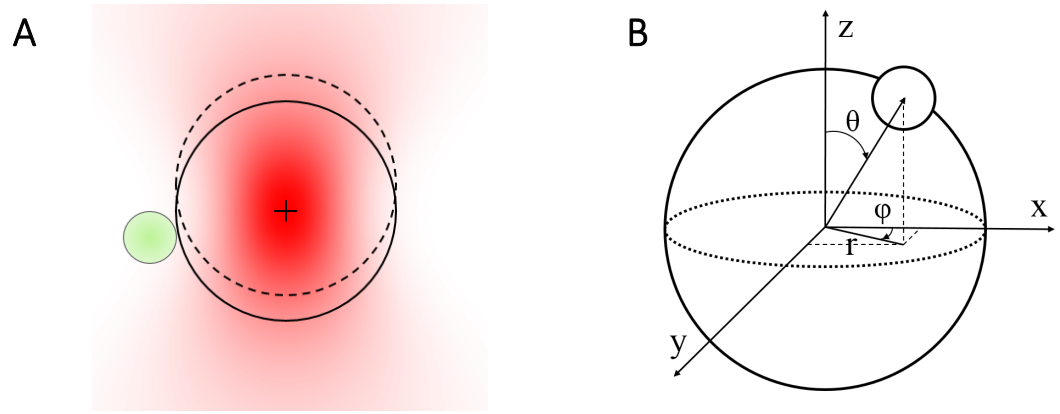

Figure 3.2. Composite bead trapped in a highly focused beam and the employed coordinate system. (A) Large bead (r = 500 nm,) and small bead (r = 100 nm) both drawn to scale at the center of the Gaussian beam (full line) and slightly behind the focal point at z_{eq} = 143 nm (dashed line). The small bead experiences highest intensity at the top and bottom of the large bead, while it is effectively outside of the Gaussian beam at $\theta = 90°$. (B) Spherical coordinate system used for the positions of the small bead.

As shown in Fig. 3.3A, the lowest intensity is experienced close to 90° polar angle (the "equator") of the large bead. This can be expected when one considers that the Gaussian beam waist is only 411 nm, while the sum of radii of the two beads is 600 nm. From the figure 3.2B, it is clear that the small bead is essentially outside of the trapping beam when close to the equator of the large bead.

To obtain the force acting on the small sphere, we use the Rayleigh limit formulas (2.2) and (2.5). Because of the rotational symmetry of the problem, we decomposed the forces into a radial force, acting in the direction perpendicular to the beam axis, and axial force, acting along the beam axis. The computed forces for beam of power 1 mW are plotted in Fig. 3.4, again as a function of the polar angle θ. As expected, the radial force (Fig. 3.4A) is always negative (i.e. points towards the beam axis), while the axial force changes sign as it transitions from the top hemisphere to the bottom hemisphere (Fig. 3.4B).

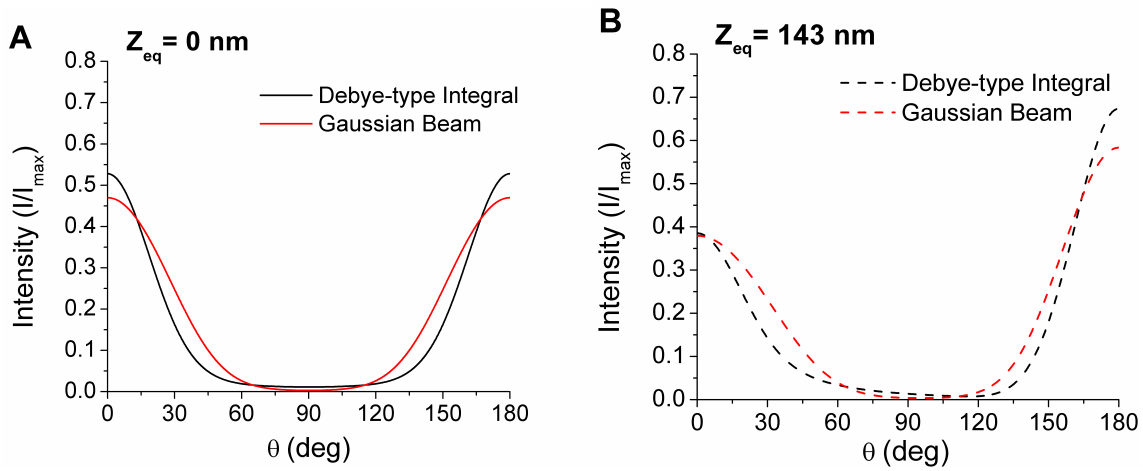

Figure 3.3. Intensity at position of the small bead as a function of polar angle for Debye-type beam (black) and Gaussian beam approximation (red). With the composite bead at center of the beam (A), equal intensity is experienced by the small bead when on top or bottom of the large bead. When the composite bead is slightly behind the center of the beam (B) the highest intensity is at the bottom of the large bead.

The situation changes dramatically when the composite bead is placed behind the focus of the trapping beam (Fig. 3.4C and D), where the small bead experiences much higher forces around the bottom of the large bead (close to 180°) than on the top. The force in the Z-direction follows a similar trend (higher force on bottom of the large sphere) albeit to a lesser degree.

Because we are interested in the rotational behavior of the composite bead we further calculate the torques exerted by the small bead on the large bead. The total torque is given by the relation $\tau_p = (a + a_p)(F_z \sin\theta - F_r \cos\theta)$, which combines the torque resulting from the radial force F_r, and the axial force F_z, where a is the large bead radius and a_p is the small bead radius. As shown in Figure 3.5, the radial force is the main contributor to the total torque exerted by the small bead.

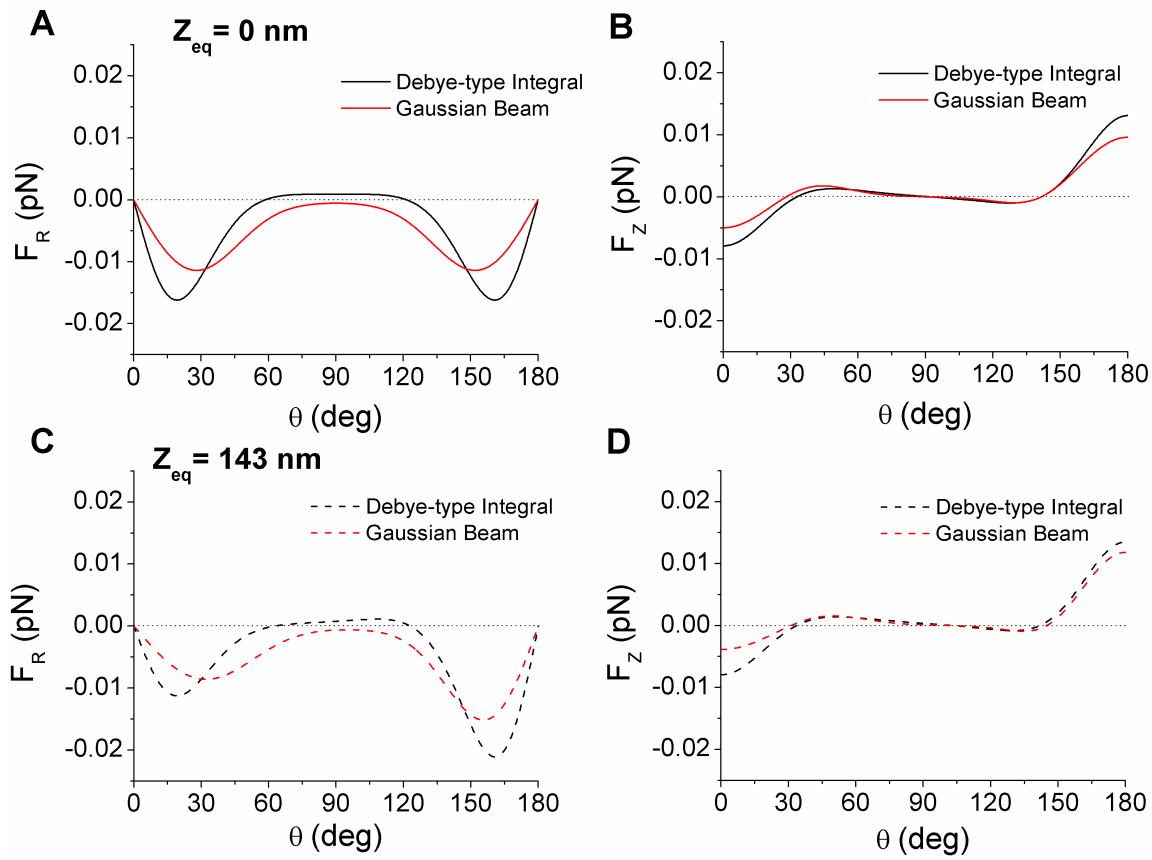

Figure 3.4. Radial and axial forces acting on small sphere as a function of polar angle. Radial (A and C) and axial (B and D) forces for Debye-type beam (black) and Gaussian beam (red) in the beam center (A and B) and with equilibrium position $z_{eq} = 143$ nm (C and D).

Finally, we integrate the torque exerted by the small bead over the radial angle θ to get the potential energy of each position. The results of the integration for the composite bead at the center of the beam (Fig. 3.6A) show that the small bead creates a rotational energy landscape with two potential wells of relatively equal depth: one for the orientation with the small bead down and one with the small bead up (from now on, we designate these states as "Down" state ($\theta = 180°$) and "Up" state ($\theta = 0°$) and the depth of these wells as ${E_{\mathrm{b1}}}^{0}$ and ${E_{\mathrm{b2}}}^{0}$, respectively). The attachment of the small bead therefore breaks the rotational symmetry of the system, as it – with sufficiently high laser power – reduces the set of microstates the system can explore.

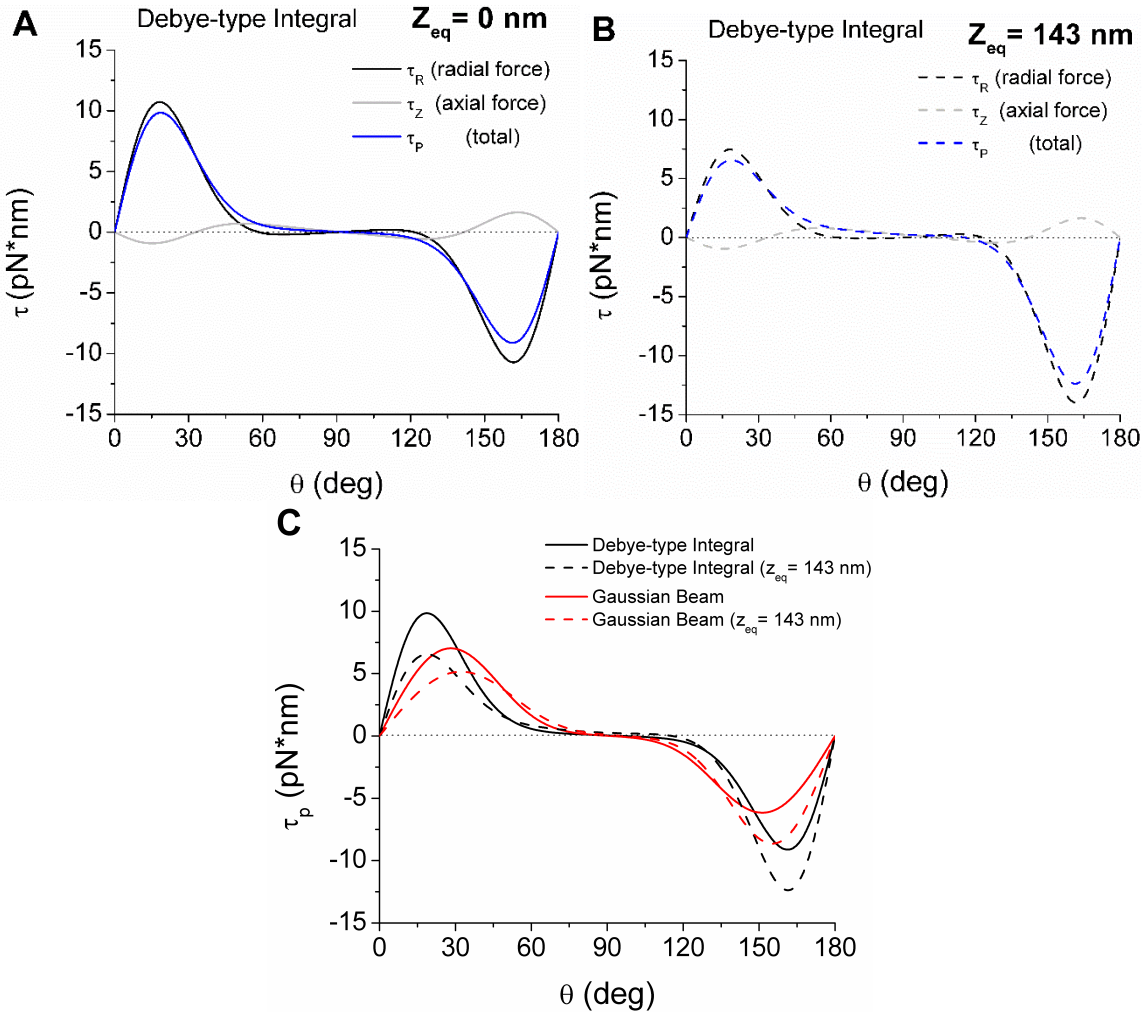

Figure 3.5. Torque exerted by the small bead as a function of polar angle. The radial force (black) is the major contributor to the total torque (blue) exerted by the small bead for both equilibrium positions, $z_{eq} = 0$ nm (solid line) and $z_{eq} = 143$ nm (dashed line).

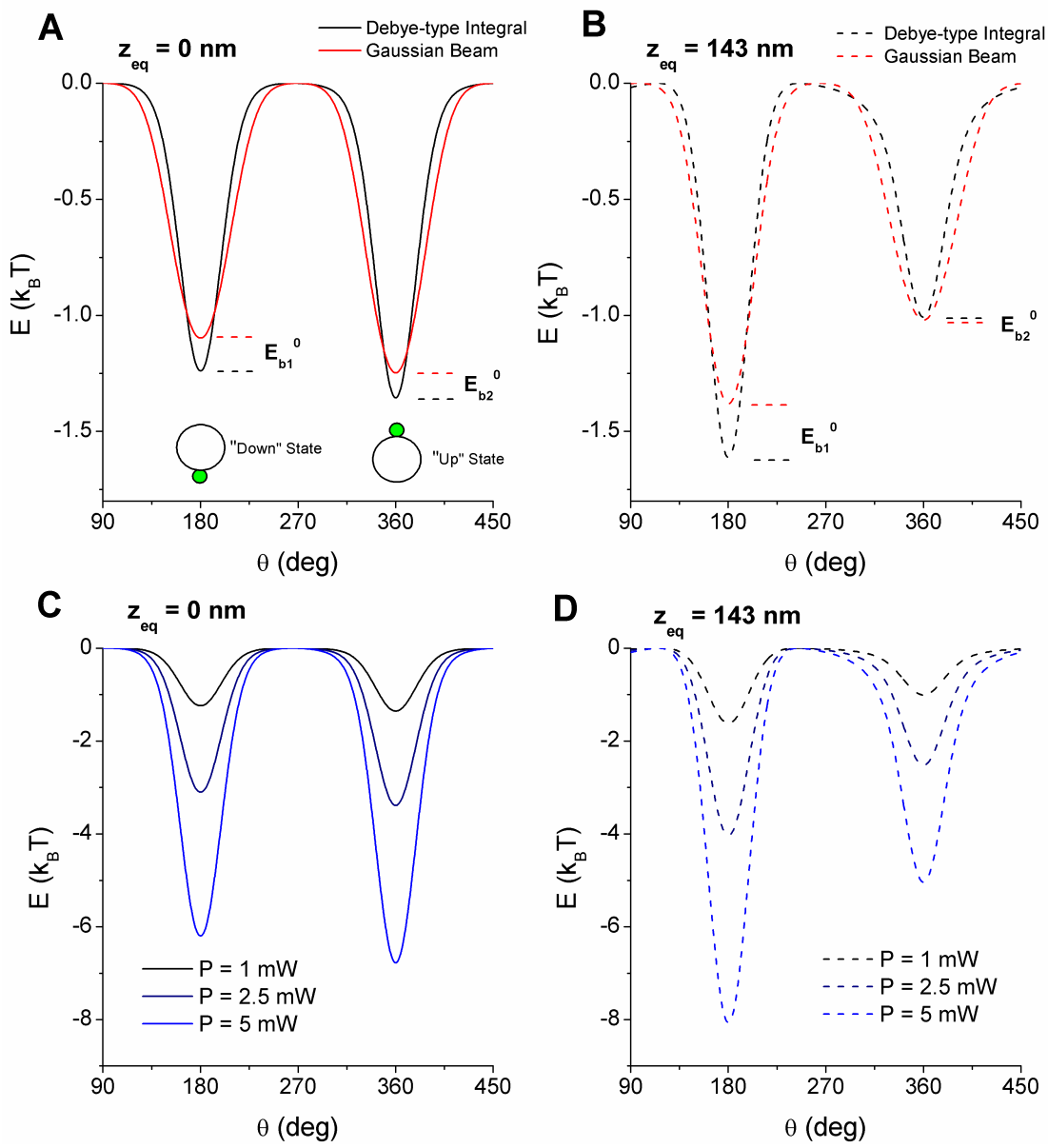

Figure 3.6. Energy landscapes of the rotational orientations of the composite bead. Attachment of the small bead creates two favorable orientations with low potential energy: the "Down" state and the "Up" state. Highlighted are the ground state energies – $E_{\mathrm{b1}}{}^{0}$ and $E_{\mathrm{b2}}{}^{0}$. With the composite bead in the center of the beam (A), the potential wells are relatively equal, with a small difference due to the radiation pressure force acting on the small bead. In the case equilibrium position $z_{eq} = 143$ nm (B), the traps become significantly unequal. The depth of the energy wells are directly proportional to the trapping beam power (C and D).

When the composite bead is in the center of the beam (Fig. 3.6A) the "Up" state has slightly lower energy. This is due to the radiation pressure force exerted on the small bead, which acts in the direction of the beam propagation (we assume beam propagating from the bottom of the bead, which corresponds to our experimental setup).

Interestingly, the potential wells have significantly unequal depth in the case of large bead positioned behind the behind the focal point (Fig. 5.4B). The intuitive explanation is that by moving the composite bead behind the focus, we expose the small bead on the bottom to a larger beam intensity (Fig. 3.4 B) and, more importantly, higher intensity gradient. This results in larger force acting against the bead when it tries to move away from the bottom of the large sphere. In the last two panels (Fig. 3.6 C and D), we show that the depths of the energy wells are linearly dependent on the beam power. In Fig. 3.7A, we calculate the ground state energies as a function of the composite bead equilibrium position z_{eq}. The results show that the energies are relatively linearly dependent on the position with opposite trends for the "Up" (${E_{\mathrm{b2}}}^{0}$) state and the "Down" (${E_{\mathrm{b1}}}^{0}$) state. The ratios of the energies are shown in Fig. 3.7B for beads of three radii: 500 nm, 600 nm and 700 nm. As we can see, the ratio of the ground state energies are also linearly dependent on the equilibrium position and, further, do not change drastically for beads of different sizes (there is virtually no difference under the Gaussian beam approximation). For this reason, we have designed an experiment to measure the ratio of the potential wells (see Chapter 6), which in turn allows us to estimate the equilibrium position.

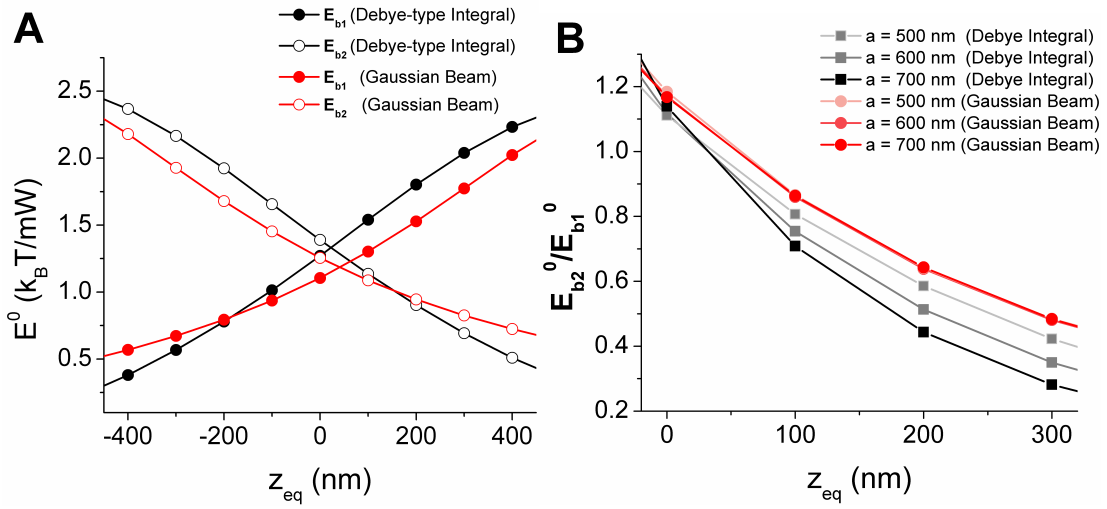

Figure 3.7. Top-down symmetry breaking as a function of the bead equilibrium position. (A) The depth of potential wells shown as a function of the equilibrium position. (B) The ratio of the two potential well decreases, as the bead is moved outside of the equilibrium. In the experimental section, we use this fact to establish the equilibrium position. We also note that the ratio is not heavily dependent on the large bead size.

As we can see throughout this chapter, the Gaussian approximation is relatively accurate even for the highly convergent beams although discrepancies do occur. Due to this reason we resort to the full Debye-type integral representation in our simulations in Chapter 3.This, however, comes at the cost of losing the simple analytical form for representing the trapping beam and resorting to numerical solutions of the equation (2.12).

We note that the only other source of torque besides the effect of the small attached beads are the thermal excitations from the environment (the laser beam is plane polarized and doesn't transfer any torque). Since the Brownian torques are of magnitude approximately k_BT, we can predict that increasing the laser power will induce a spontaneous symmetry breaking in the system.

CHAPTER 4

BROWNIAN DYNAMICS SIMULATION

Using the theoretical results from the preceding chapter, we implement a Brownian dynamics simulation to investigate the rotational behavior of the composite bead as a function of laser power. The simulation is based on the Smart Monte Carlo (SMC) algorithm [45] and employs the formulas for calculation of forces in optical trap introduced in Chapter 3. The chapter is divided in the following sections: 1) introduction of Langevin dynamics 2) details on the simulation code and 3) results of the simulation.

Langevin Dynamics

The composite bead is a subject to random thermal excitations from the environment, resulting in a Brownian motion. At low Reynolds number, the inertial effects can be neglected and the particle dynamics are be described by the overdamped Langevin equation [46]:

$$\zeta \frac{dx}{dt} = -\frac{\partial U}{\partial x} + f(t) + \frac{\zeta}{2}\frac{\partial D}{\partial x} \tag{4.3}$$

where U is an external potential, ζ is the friction constant and $f(t)$ is the sum of random forces due to the collisions with molecules in the surrounding fluid. The last term in Eq. 4.3 accounts for dependence of the diffusion constant D on [47]. As mentioned, this equation neglects the inertial effects under the assumption that $\zeta/m \gg 1$, where m is the mass of the particle. The friction constant ζ is indirectly proportional to the diffusion constant D through the Einstein's relation

$$D = \mathrm{k_B T}/\zeta \tag{4.4}$$

and the inverse of friction constant $1/\zeta$ designates the mobility of the particle.

The equivalent of Eq. 4.3 in a multidimensional space with 3 translational and 3 rotational degrees of freedom is given by:

$$\frac{dx_n}{dt} = \sum_m L_{nm}\left(-\frac{\partial U}{\partial x_m} + f_m(t)\right) + \frac{1}{2}k_B\mathrm{T}\sum_m \frac{\partial}{\partial x_m}L_{nm} \tag{4.5}$$

where L_{nm} is the 6x6 mobility matrix relating the drag force and velocity along the individual dimensions. The Einstein's relation connecting the mobility matrix to the diffusion matrix in multidimensional space is analogous to (4.4): $L_{nm} = D_{nm}/k_BT$. In our calculations we assume that the diffusion matrix D_{nm} is independent of the particle position x, which corresponds to a freely suspended particle in homogeneous media, allowing us to drop the last term in (4.5). This approximation is justified, since the distance to surface in our experiments is 1 μm, at which the surface effects are negligible [48]. Further, we assume that the matrix D_{nm} is diagonal (i.e. the degrees of freedom are decoupled), which enables us to solve the problem in each dimension separately.

The implemented algorithm is based on finite step integration of the equation (4.5)

$$x_n(t+\Delta t) = x_n(t) - \sum_m L_{nm}\frac{\partial U}{\partial x_m}\Delta t + g_n(\Delta t) \tag{4.6}$$

where $g_n(\Delta t)$ is a random variable drawn from a Gaussian distribution with first and second moment defined by $\langle g_m(\Delta t)\rangle = 0$ and $\langle g_n(\Delta t)g_m(\Delta t)\rangle = 2D_{nm}\Delta t$, respectively.

Details of the Simulation Code

The SMC simulation is implemented in Matlab (MathWorks, USA). Before running the simulation, we calculate the trap spring constants from the electrostatic approximation (Appendix A), which allows us to calculate the forces acting on the large sphere. To get the forces acting on the small bead, we numerically pre-calculate the Debye-type intensity field as a 2D function of radial and axial distance with approx. 5 nm grid size (Eq. 2.12). We then compute the gradient of the field and use equations (2.2) and (2.5) to calculate the force fields in radial and axial direction as a function of radial and axial position. Due to the rotational symmetry of the problem, this force field can be used for any position of the small bead in 3D space.

At the beginning of each step, we calculate the forces acting on both of the spheres: the forces on the large sphere are calculated from the two spring constants and the forces on small beads are calculated by 2D interpolation from the pre-calculated force field, based on the current position of the small bead. We note that the small bead position takes into account the displacement of the large bead with respect to the center. The torque exerted by the small bead about each of the coordinate axis is then calculated using triple product:

$$\boldsymbol{\tau}_n = \boldsymbol{n} \cdot (\boldsymbol{r} \times \boldsymbol{F}) \tag{4.6}$$

where $\boldsymbol{n}$ is the unit vector in the direction of the given coordinate axis, $\boldsymbol{r}$ is the current small bead position with respect to the large bead center and $\boldsymbol{F}$ is the force acting on the small bead. The composite bead is then translated and rotated using the force and torque input from both beads and random input from the environment (Eq. 4.5). Each step is then accepted or rejected based on the SMC criteria [45].

To speed up the calculation, we use the very fast Matlab function "griddedInterpolant.m" to interpolate the values from the force fields using a spline method. The random numbers are generated by the function "randn.m". Currently, the

simulation code runs very efficiently, allowing us to simulate the bead behavior faster than in real time on our desktop PC (Intel Core i5-2400 @3.1GHz), with the bottleneck being the calculation of the triple product in Eq. 4.6.

The parameters used in the simulation were selected to match our experimental conditions: temperature 23°C, wavelength in medium $\lambda = 806$ nm, beam waist width $w_0 = 411$ nm, large bead radius $r_l = 600$ nm and small bead radius $r_s = 100$ nm and the equilibrium position $z_{eq} = 143$ nm (see Chapter 6 for details on estimation of the equilibrium position). Because we used polystyrene spheres as the small beads in our experiments, we use the refractive index $n_2 = 1.57$ (this is a slightly different value from Chapter 3, which assumed a glass material with $n_2 = 1.52$ for both beads). The time step of the simulation ($t = 0.3$ ms) was chosen to be lower than the translational and rotational time scale, with the exception of the highest simulated power (20 mW), where the time scale of the translational motion is ~ 0.2 ms due to the relatively high spring constant in the lateral direction (0.057 pN/nm). Even in this case, the SMC step rejection rate is < 38%, which is still acceptable.

Results of the Simulation

In the following section I present the results of the simulation. We ran the simulation from two starting orientations – with the small bead on top ($\theta = 0°$) and bottom ($\theta = 180°$) – for multiple different laser powers from 1 mW to 50 mW (we note that this is the laser power of the beam after passing the objective). Each simulation was run for 50 minutes of simulation time. The results of individual simulation runs are shown in Fig. 4.1. The figure very well captures the symmetry breaking, as the number of possible microstates of the system decreases with increasing laser power. At 5 mW, we still observed transition from the bottom potential well, to the top, however, at 7.5 mW, only transition from top to bottom was observed.

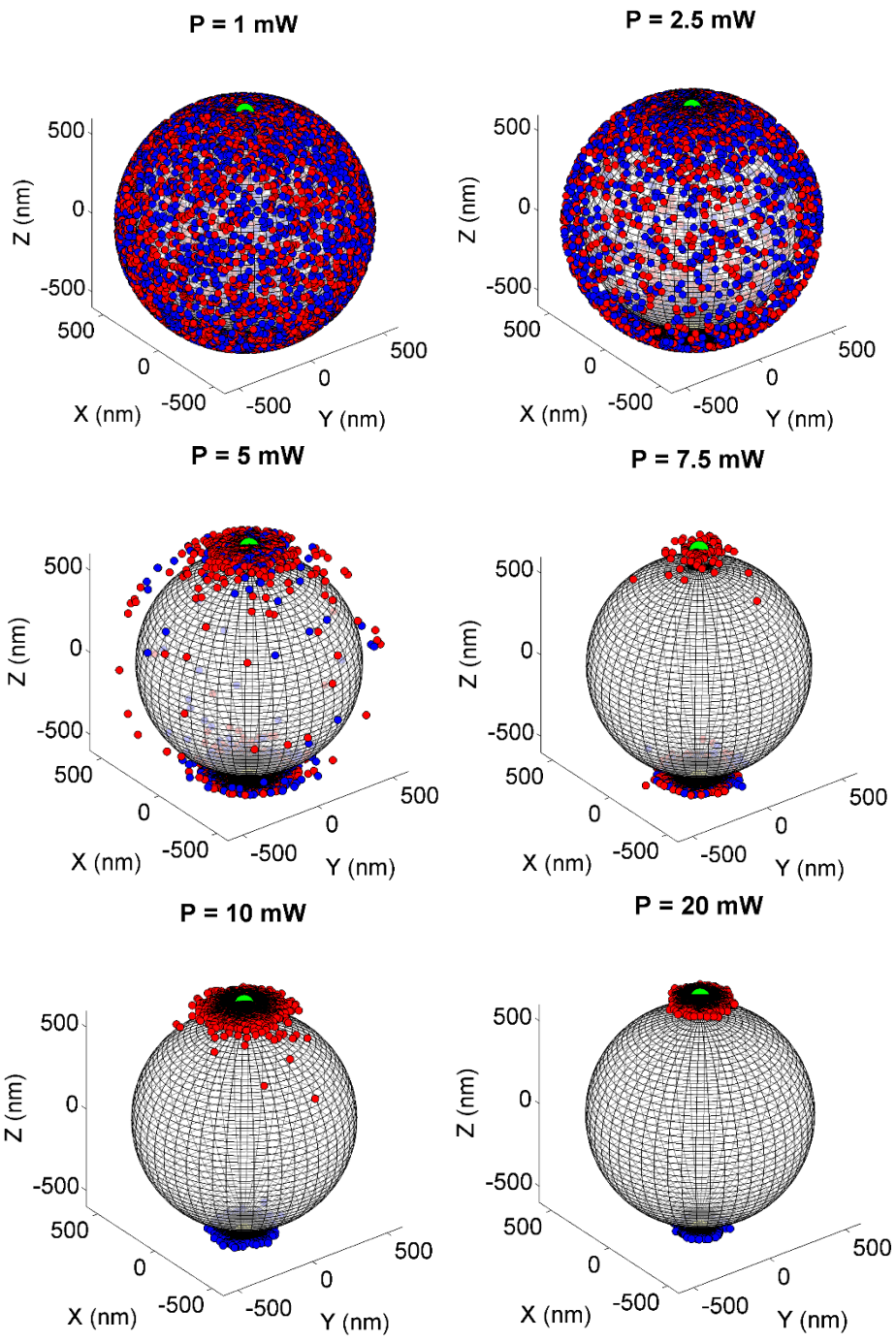

Figure 4.1. Brownian dynamics reveals spontaneous symmetry breaking for increasing laser power. In each panel we plot the results of two 50 minute runs of Brownian dynamics simulation, starting from "Up" position (red dots, green point represents the starting position) and "Down" position (blue dots). Each dot represents a snapshot of the small bead position after 9 seconds of simulation time.

A more quantitative analysis of the small bead positions is shown in Fig. 4.2, where we plot histogram of the small bead positions as a function of polar angle θ weighted by the appropriate surface area of the sphere. For the 1mW beam power a quite uniform distribution is present, which is suppressed at higher trapping beam powers, as the probability density concentrates more and more around the north and south pole of the large bead. At 10 mW power, we plot two simulation results, each with different starting position, since no transition between the "Up" and "Down" states occurs at this power.

Not surprisingly, the Brownian dynamics simulation behaves according to the predictions of the theory in Chapter 2. We show that increasing of the laser power can indeed produce a symmetry breaking even when taking into account the translational motion of the composite bead. The only unknown parameter in this section is the equilibrium position of the composite bead, which is experimentally determined in Chapter 6 by measurement of the ratio of the two potential wells as well as their depth.

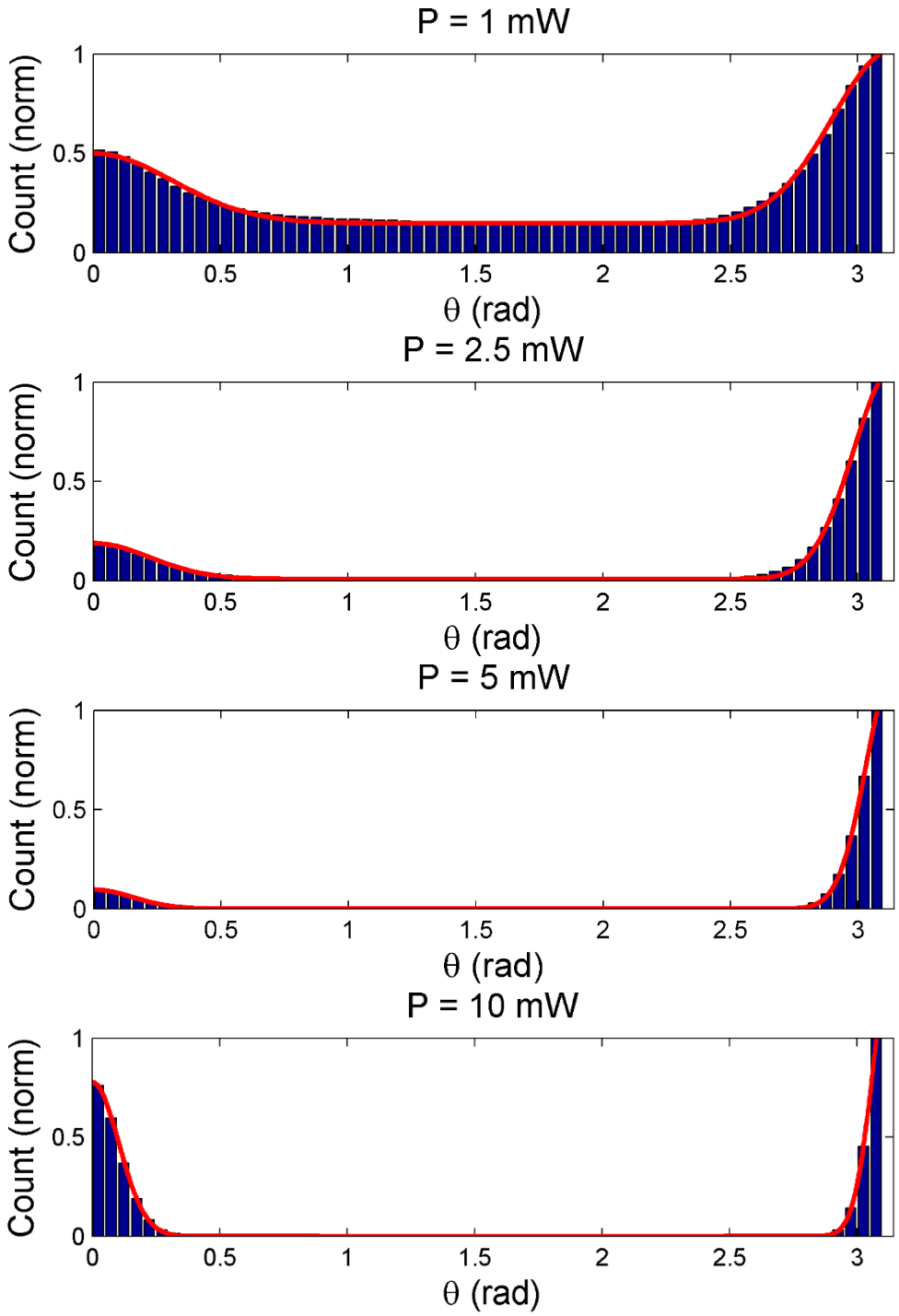

Figure 4.2. Normalized histograms of small bead positions as a function of polar angle. At the lowest power, an almost uniform distribution of the rotational orientations is observed at 1 mW power. As the power is increased, the small beads gets more and more confined to the poles of the large bead. Red line represents two fitted half-Gaussians, centered at $\theta = 0°$ and $\theta = 180°$.

CHAPTER 5

MATERIALS AND METHODS

In this section, I describe the experimental setup used to verify our theoretical predictions. In the first part, I provide brief description of the optical tweezers instrument, followed by a protocol for preparation of the composite beads and verification of the attachment. The second part of this chapter describes the algorithm for tracking of the composite beads and calibration of the instrument. The last part is designated to presentation of a novel algorithm for tracking of the rotational motion of the composite beads.

Optical Tweezers Setup

The basis of the optical tweezers setup is described in previous publication [48]. Briefly, the optical trap is created by passing 500 mW Nd:YAG 1064 nm CW diode laser (Compass 1064-500, Coherent Inc., Santa Clara, CA) through liquid crystal power controller (Brockton Electro-Optics Corp., Brockton, MA) and a beam expander (2–8×, Special Optics, Wharton, NJ) (Fig. 5.1). The beam is then focused by 100×/1.3NA oil immersion objective (Carl Zeiss, Inc., Thornwood, NY), which is mounted on a Zeiss Axiovert S100 inverted microscope. The bead is simultaneously illuminated by 100W halogen lamp and imaged through the same objective onto two 12 bit CCD cameras (SensiCam, Cooke Corp., Auburn Hills, MI and GE680, Prosilica, MA). The data from the SensiCam camera is collected at 70 frames per second and analyzed by a custom software implemented in LabVIEW 6.5 (National Instruments Corp., Austin, TX) to provide online tracking of the trapped microsphere. Data from the Prosilica camera is collected at maximum 600 frames per second and saved for offline analysis. Both of the

videos are typically 100 by 100 pixels in size, covering the entire image of the trapped bead.

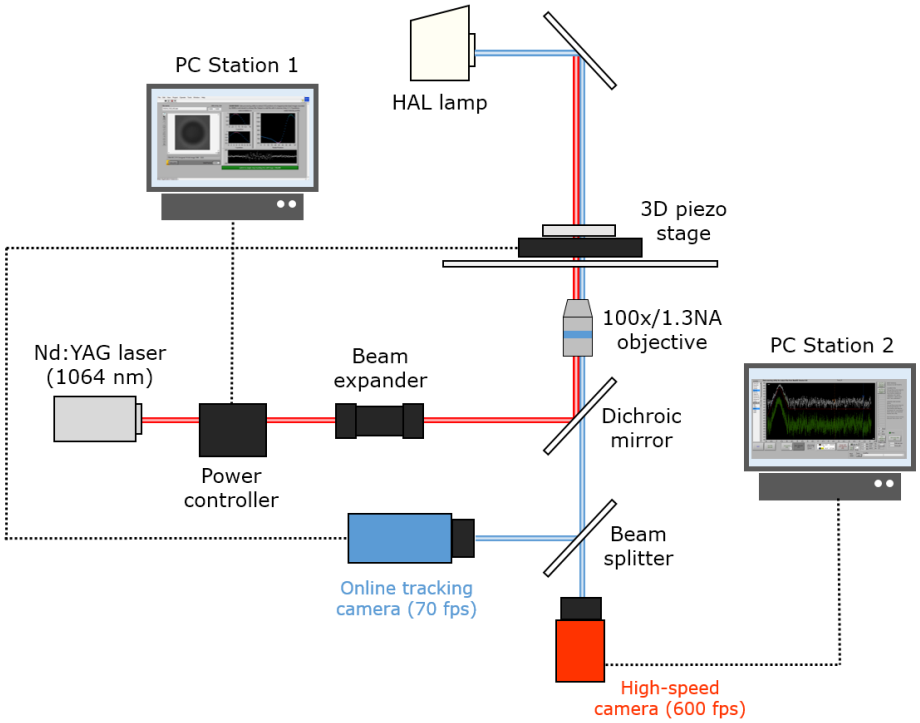

Figure 5.1. Schematic of the optical tweezers. The laser beam (red) is passed through power controller and beam expander. The trap is created by focusing the expanded beam through high NA objective. The bead is imaged through the same objective by two cameras using visible light from halogen lamp. One of the camera is used for online tracking at lower frame rate (blue) and one high-speed camera for offline analysis (red).

Composite Bead Preparation

The composite beads were prepared by attaching 200 μm diameter yellow-green fluorescent polystyrene beads with biotin surface modification (FluoroSpheres 505/515, Molecular Probes, Eugene, OR) to borosilicate glass microspheres (Duke Scientific, Palo Alto, CA) through biotin-streptavidin linkage. The glass microspheres were first cleaned with boiling base piranha solution (mixture of 30% hydrogen peroxide and concentrated

NH_4OH) and conjugated with mercaptosilane groups (3-mercaptopropyltrimethoxysilane, MPTMS) (United Chemical Technologies, Bristol, PA). In a separate tube, streptavidin was covalently linked with heterobifunctional polyethylene glycol (MAL-PEG3500-NHS, Sigma-Aldrich, St. Louis, MO) in Carbonate-Bicarbonate buffer (pH 8.5) (30 minutes incubation).

The pegylated streptavidin was mixed with the MPTMS beads and the pH was adjusted to 6.9 with phosphate buffer, resulting in conjugation of maleimide to a sulfhydryl groups on surface of the bead. After 5 hour incubation at room temperature, the Streptavidin-coated beads were washed six times with HEPES buffer (pH = 7.4) by spinning down in tabletop centrifuge at 18 000 rcf and kept at 4 °C. In the last step, streptavidin coated borosilicate beads were mixed with the biotin coated polystyrene beads and incubated overnight at room temperature. The final suspension containing linked borosilicate and polystyrene beads was washed three times in HEPES buffer (pH = 7.0) and kept at 4 °C.

The attachment of the polystyrene and the borosilicate beads was verified by fluorescence microscopy (Fig. 5.2). Similarly, we verified that only a single small sphere was attached in beads used in experiment by collecting a Z-stack of the composite bead.

To avoid adhesion of the composite beads to bottom of the microscope chamber, the cover glass of the trapping chamber was first cleaned with boiling base piranha solution and incubated with BSA (0.5% in HEPES, pH = 7.0) for 30 minutes at room temperature. Before using, the chamber was washed 3 times with HEPES buffer.

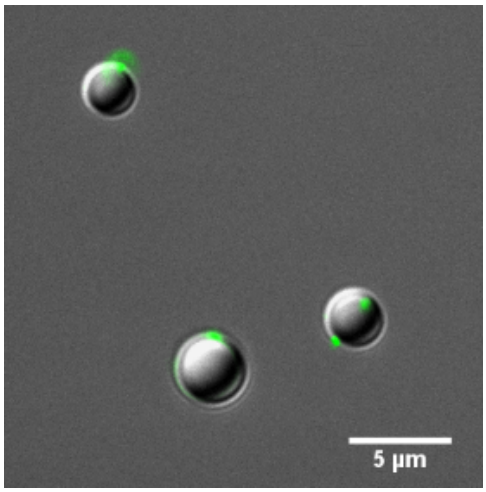

Figure 5.2. Overlaid difference interference contrast and fluorescence image of composite beads. The 200 µm diameter yellow-green fluorescent polystyrene beads (green) were attached to the borosilicate beads through biotin-streptavidin linkage.

Large Bead Tracking Algorithm and Spring Constant Calibration

The 3D positions of the ~ 1 µm diameter borosilicate bead are extracted through offline processing of the images. First, the rough XY position is established through center of mass of the image intensity gradient. The center is then refined to subpixel accuracy using cross-correlation of mirrored images [49]. The Z tracking is based on a distance between intensity maximum and minimum in the radial profile of the bead (Fig. 5.3) [48]. This metric, which is linearly dependent on the distance from the focal plane, requires an independent calibration procedure for each bead. During calibration, the piezo stage is repeatedly elevated and retracted with a constant speed, pushing the trapped bead out of focus (Fig. 5.3C). The Z calibration is determined by manually matching the slopes of the Z positions of the bead and the piezo stage in post processing. The tracking algorithm accuracy (established by tracking a surface immobilized microsphere on moving piezo stage) is within 2 nm in transversal directions and 5 nm in axial direction (standard deviations).

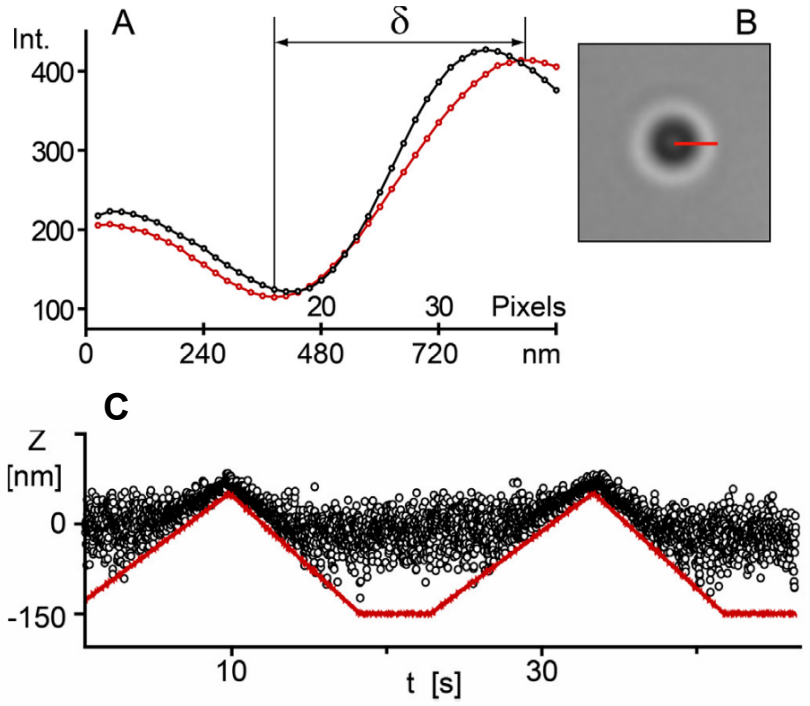

Figure 5.3. Tracking algorithm for positions of the large bead (adapted from [48]). The tracking in Z direction is based on an interference pattern formed by the trapped microsphere. The distance between the local maxima and local minima of radially averaged intensity δ (A, B) is linearly proportional to the elevation of the bead. The calibration of this metric is achieved by approaching and retracting the piezostage with precisely defined speed and then matching of the two slopes (C).

The spring constants κ_i are determined from the equipartition theorem:

$$\kappa_i = \frac{k_B T}{{\sigma_i}^2} \tag{4.1}$$

where σ_i is a standard deviation of the bead positions along dimension *i,* after correcting for motion blur caused by finite acquisition time of the camera [50] and random tracking error. Shown in Figure 4.4 are the spring constants measured by our instrument for a 0.6 μm diameter bead under various laser powers.

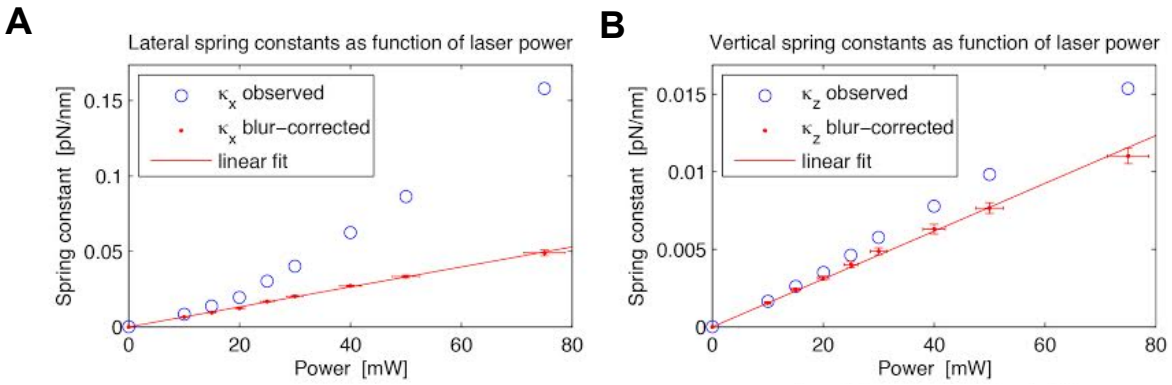

Figure 5.4. Spring constants for varying laser power. (A) Lateral (B) axial spring constants show linear dependence on laser power after correcting for motion blur.

Small Bead Tracking Algorithm

The position of the small bead (or, equally, the rotational orientation of the composite bead) is determined through a multi-step image processing algorithm. Although the small bead in our experiments falls below the diffraction limit, we were able to observe its diffraction pattern as a very faint spot superimposed on the image of the large bead (Fig. 5.7 (Supplementary Video S1)).

Interestingly, the faint spot was clearly visible only when the small bead was in the "Up" position (i.e. away from the objective). We tested this observation by trapping the composite bead at a relatively high laser power (50 mW) and approaching and retracting the stage. In Figure 5.5, two traces with small bead in "Up" and "Down' states are shown. With the small bead in the "Up" state (the faint spot is observable), the large bead positions closely follow the displacement of the stage, with equal slopes of both traces (green and red). In the second scenario (small bead on the bottom), the large bead is displaced by the stage at much larger distance, with unequal slopes between the traces. This is most likely due to the small bead initially pushing the composite bead up and eventually being displaced sideways under the force of the large sphere towards the stage surface. This implies that the small bead is indeed at the bottom of the large bead.

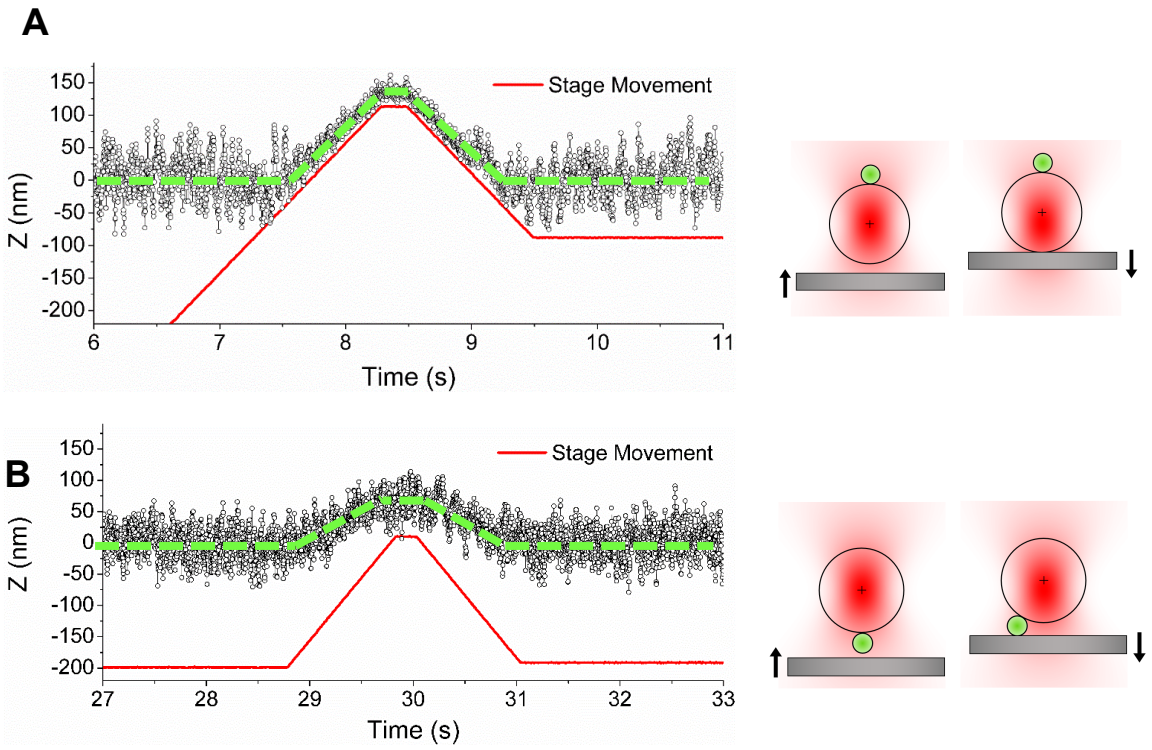

Figure 5.5. Traces of large bead positions with small bead in the "Up" (A) and "Down" (B) states when captured at high laser power (50 mW) and displaced by the movement of the piezostage (red line). (A) With the small bead in the "Up" position, the large bead displacement (green) closely follows the motion of the stage. (B) With the small bead present at the bottom of the large sphere, the effects of stage motion are apparent at much larger distance, with the stage and the large bead moving at different velocities (slopes). This implies that the small bead is in the "Down" state.

Since the trapped composite bead is a subject to random Brownian torques as well as torques imposed by the attached small bead, it explores different rotational states over time. We can therefore calculate the average image over sufficiently long time and effectively average out the diffraction pattern of the small bead. The average image is calculated from relevant segments of the recording, aligned using the XY position of the large bead (established by the large bead tracking algorithm introduced in previous section).

In second step, the average image is subtracted from the individual aligned frames. While the small bead is very faint in the raw image, it can be readily discerned after subtracting the average image (Fig. 5.6 Row 2, Fig. 5.7 (Supplementary Video S1)). After subtraction, the images are processed with median filter to reduce noise (Fig. 5.6 Row 3).

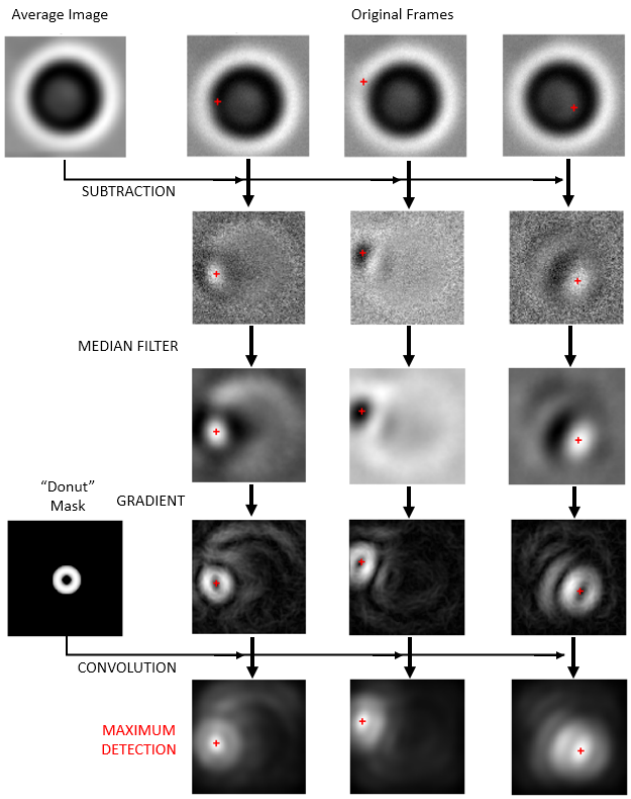

Figure 5.6. Image processing algorithm for detection of the small bead position. In the first step, the average image – calculated from sufficiently long segment – is subtracted from each of the original frames (Row 2) and the resulting images are median filtered (Row 3). In the second step, gradient of the median filtered images is calculated and convolved with a "donut" mask defined by torus equation (Eq. 4.2). In the last step, maximum of the convolved image is found and used as the small bead position.

While the position of the small bead is usually apparent to a human observer, the image doesn't have a uniform appearance from frame to frame (see Fig. 5.6), which makes it a challenging subject for image processing. We achieved the best results by the following algorithm: first, we calculate the spatial gradient of the median filtered image (Fig. 5.6, Row 4, Fig. 5.8 (Supplementary Video S2)) and convolve the gradient with a "donut mask" defined by torus equation

$$\left(R_t - \sqrt{x^2 + y^2}\right)^2 + z^2 = {r_t}^2 \tag{4.2}$$

where R_t = 9 px and r_t = 5 px are the major and minor radius, respectively (see Figure 5.6, Row 4). In the last step, we find the maximum of the convoluted image (Fig 5.6, Row 5). With this algorithm we achieved fairly robust results in detecting the small bead position.

To improve the tracking algorithm, we take advantage of the high temporal resolution of our data to further improve the accuracy of the small bead detection. Since the frame rate in this experiment is very high (~ 600 frames per second), we penalize large displacements of the small bead, which are very unlikely to occur within the time interval between individual frames. Specifically, we impose the limit of maximum distance travelled by the small bead from frame to frame to 30 pixels (~ 0.6 μm). If the detected maximum falls outside of this range, the current frame is temporarily skipped and the next frame is analyzed, this time with 40 px region etc. For the frames with tracking error, the small bead position is retrospectively calculated by linear extrapolation between the neighboring frames.

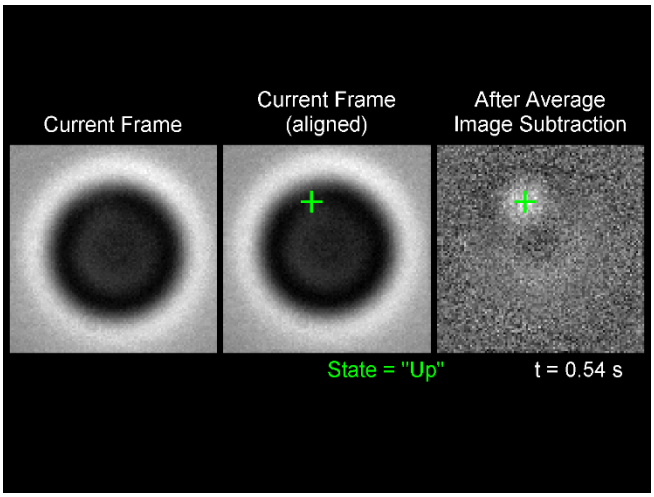

Figure 5.7 Video of composite bead captured in optical trap. The composite bead undergoes Brownian motion in optical trap (left). In first step of the tracking algorithm, we align the images using cross-correlation (center). The aligned images are then averaged over relevant part of the recording and subtracted from the current image, highlighting the position of the small bead (right). Highlighted by colored cross is the current position of the small bead in either "Up" (green) or "Transition" state (blue). The tracking algorithm is accurate only for those two states and therefore no cross is shown for the "Down" state. (S1_Supplementary_Video.avi, 19,540 KB)

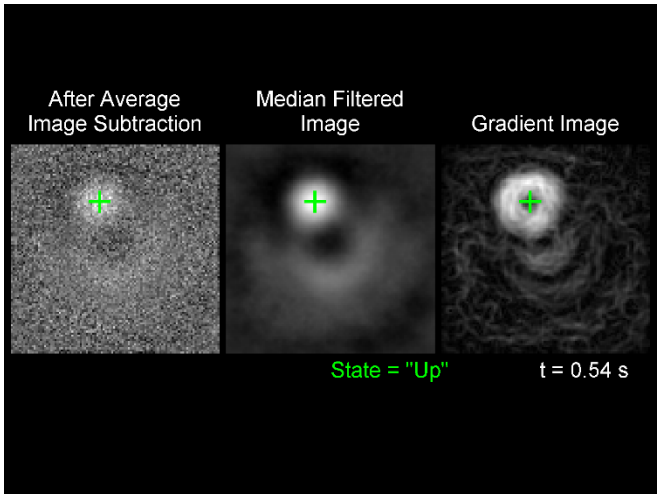

Figure 5.8 Video of algorithm for tracking of rotation of the composite bead. After subtraction of the average image (left) (see Fig. 4.4 and Video S1), we apply median filter to remove noise (center) and calculate the gradient magnitude of the image (right). In the next two steps, we convolve the gradient image with a "Donut" mask, defined by torus equation and look for the maximum of the result of the convolution (both steps not shown), which corresponds to the small bead position and is is highlighted by colored cross. (S2_Supplementary_Video.avi, 18,190 KB)

CHAPTER 6

EXPERIMENTAL RESULTS

In this chapter, we experimentally confirm and quantify the theoretical predictions. We design two experimental procedures that allow us to estimate two critical parameters: the equilibrium position of the composite bead and the power of the beam after passing the objective. In the first experiment, designated as the power ramp experiment, we estimate the ratio between the two potential wells based on thermally activated transitions between the two states. The second experiment uses the small bead tracking algorithm to measure the extent of the small bead confinement under various powers.

Power Ramp Experiments

From the Brownian dynamics simulation results, we can predict that under sufficiently low beam power, the composite bead will exhibit transitions between the "Up" and "Down" states, resulting in a bistable two-state system. The power ramp experiment is designed to quantitatively analyze and compare the depths of potential wells in both "Up" and "Down" state, based on Kramer's reaction rate theory [51]. During the experiment we slowly lower the laser power and detect time when the first transition occurs. Lowering the laser power effectively decreases the depth of potential wells, which allows us to measure the forward kinetic rate at any moment.

Initially, the composite bead was arrested in "Up" or "Down" rotational state by high laser power (100 mW) for 2 seconds, which ensures identical starting orientation for all of the experiments starting from both "Up" and "Down" state. After the initial arrest, the laser power was set to 20 mW and linearly lowered to 10 mW over 60 s or 120 s period. Once a transition to the opposite state was detected by an online tracking

algorithm (described below) or the full time was reached, the composite bead was arrested again by high laser power (Figure 6.1, A) (we note that the laser powers in this chapter correspond to the trapping beam before entering the objective).

To detect transition from one state to another, we use a specific metric which takes advantage of the fact that – as mentioned in the Chapter 5 – the diffraction pattern of the small bead can be observed as a faint spot of higher intensity superimposed on the large bead diffraction pattern. Because this spot is much more apparent in the "Up" state, we compute the sum of the first 15 radial intensities of the angle-averaged radial intensity (Fig. 5.3), which correspond to circular region of radius ~ 360 nm around the bead center. Two typical traces of the intensity metric are shown in Fig 6.1.

In the arrest segments (Fig 6.1, magenta and cyan) the small bead oscillates in much deeper potential wells (i.e. closely around the center of the trapping beam). Due to this fact, the intensity metric is significantly higher in those segments. The "Up" (magenta) and "Down" (cyan) states can be readily discerned as the "Up" states has relatively higher intensity (Fig. 5.1 B and C), in accordance to our observation that the small bead diffraction pattern is more apparent in the "Up" state.

A typical intensity metric trace for transition from "Down" state to "Up" state shows sudden increase in the intensity signal (Fig. 6.1B, blue line) and, similarly, a transition from "Up" state to "Down" state shows sudden decrease in the intensity metric (Fig. 6.1C, blue line). Because the raw data from the intensity metric is very noisy, we employ a 41-piont moving average filter (Fig. 6.1B and C, red line).

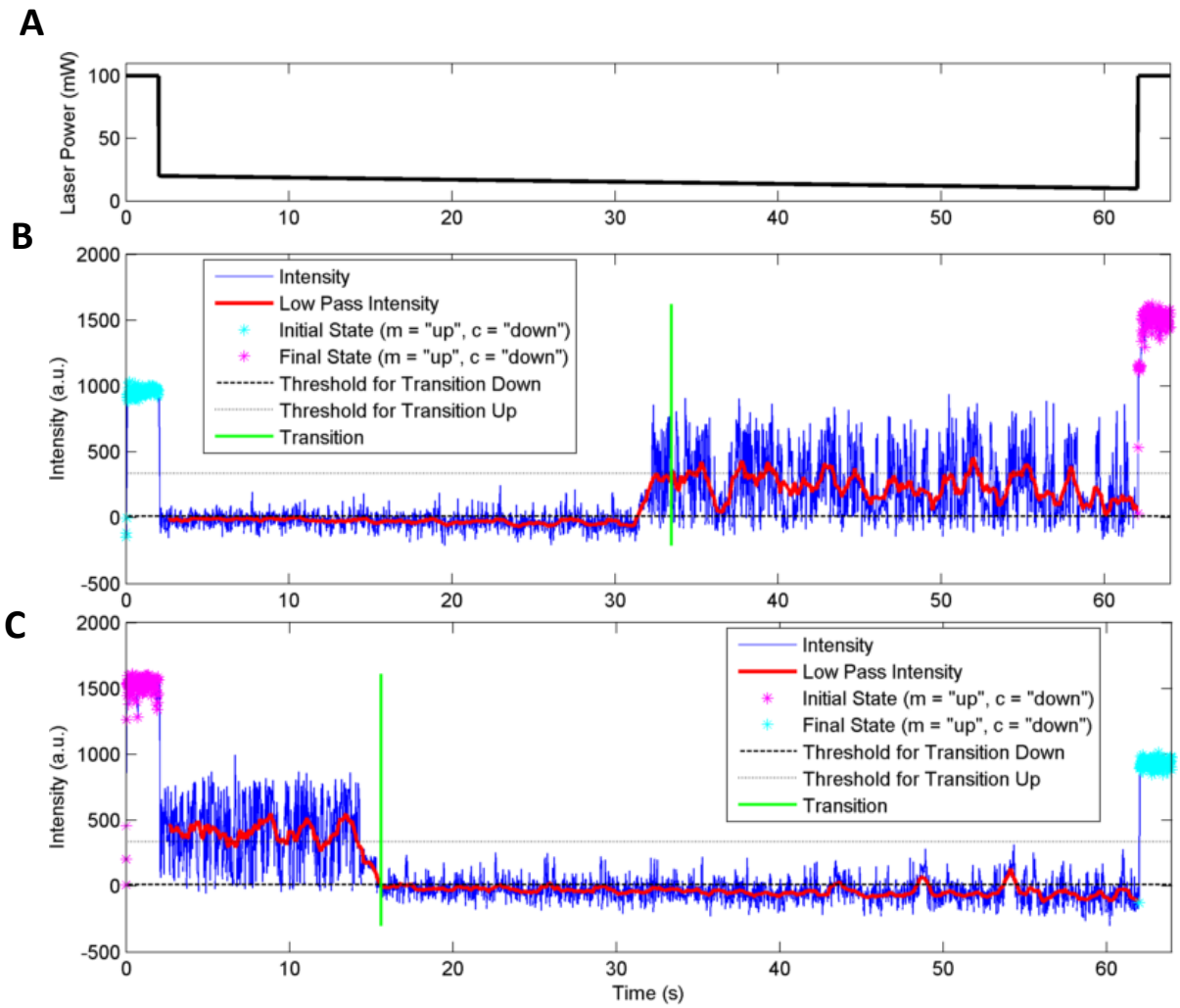

Figure 6.1. Power ramp experiment. (A) The laser power of the laser beam (before entering the objective) during the experiment. The cycle starts with 2 second high power "arrest" segment (100 mW), followed by 60 s or 120 s (not shown) linear ramp from 20 mW to 10 mW, after which another high power 100 mW "arrest segment" is applied. (B) Typical trace for transition from "Down" (cyan) state to "Up" (magenta) state, which is accompanied by abrupt increase in the intensity metric. Raw data (dark blue) is filtered by 41-point sliding average (red). Once the averaged intensity signal reaches the threshold for the transition up (shown in gray) an event is detected (green). (C) Typical trace for transition from "Up" state to "Down" state. In this case, transition is detected upon reaching the threshold for transition down (dashed black line).

We use two separate thresholds to detect the transition up and down. To obtain the thresholds, we first pool data from the first five seconds of all of the ramp phases and plot them as histograms (in these segments, we expect the small bead to reside mostly in the "Up" or Down" states, rather than the transition region). The data is fitted with two Gaussians using the maximum-likelihood estimation (MLE) (Fig. 6.2). Finally, the thresholds are selected at the level of one standard deviation of the fitted Gaussians. Therefore, to transition down from the "Up" state, the intensity trace has to drop to within one standard deviation of the down state Gaussian and vice versa.

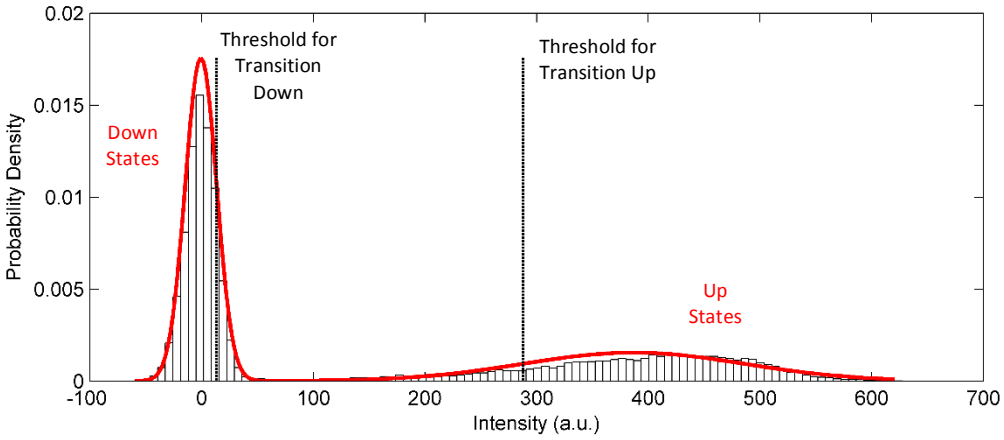

Figure 6.2. Histogram of intensity metric for detection of Up and Down states. The histogram data is pooled from 5 second segments right after initial high power arrest phase. To calculate the transition thresholds, the data is fitted by two Gaussians: one representing the "Down" state, second representing the "Up" state. The thresholds are selected as a one standard deviation from the mean of the fitted Gaussians.

In the following part of this section, I briefly describe the theory used to analyze the experimental data. As mentioned earlier, the analysis of the transition data is based on the Kramer's theory, assuming two-state system. The probability of the initial state $P_s \cong N(t)/N_{\mathrm{T}}$, where N_{T} is the total number of experiments performed, is defined as the

probability that the composite bead remains in the initial state over the course of the experiment. The temporal evolution of the system between the two states is characterized by a first-order Markov equation

$$\frac{dP_{S1}(t)}{dt} = -k_{\rightarrow}(t)P_{S1}(t) + k_{\leftarrow}(t)[1 - P_{S1}(t)] \tag{6.1}$$

where $k_{\rightarrow}(t)$ and $k_{\leftarrow}(t)$ are the instantaneous frequencies of forward and reverse transitions, respectively. Because only the initial passage is detected in our experimental setup, we can approximate the reverse transition rate as $k_{\leftarrow}(t) \sim 0$. This simplifies the two-state dynamics to a first-order decay dynamics

$$\frac{dP_S(t)}{dt} \cong -k_{\rightarrow}(t)P_S(t) \tag{6.2}$$

The solution to equation 6.2 provides the cumulated frequency of transitions

$$P_S(t) = \exp\left\{-\int_0^t k_{\rightarrow}(t')dt'\right\} \tag{6.3}$$

Using the Arrhenius' equation for the kinetic rate allows us to incorporate the energy into the relation

$$k_{\rightarrow}(t) = k_0 \exp\left\{-{E_{\mathrm{bs}}}^0 + \Delta E_{\mathrm{bs}}(t)\right\} \tag{6.4}$$

Here, ${E_{\mathrm{bs}}}^0$ is the depth of the energy well and $\Delta E_{\mathrm{bs}}(t)$ designates the change in energy well depth over the course of experiment, defined as

$$\Delta E_{\mathrm{bs}}(t) = {E_{\mathrm{bs}}}^0 c_{\mathrm{p}} \frac{t}{\Delta t} \tag{6.5}$$

where $c_{\mathrm{p}} = P(\Delta t)/P(0)$ is the ratio of laser power at the end of the ramping phase of the experiment (t = Δt) and laser power at the beginning of the experiment.

The k_0 is an "attempt" frequency, which can be calculated from equation as $k_0 = \Omega_0\Omega_{\mathrm{TS}}/2\pi f_r$, where Ω_0 and Ω_{TS} are the square roots of the second angular derivatives of the potential energy landscape at the ground state and the peak of the transition state $\left(\sqrt{\partial^2 E_{0,TS}/\partial\theta^2}\right)$, respectively, and f_r is the rotational drag coefficient, given by Stokes equation as $f_r = 8\pi\eta R^3$, where η is the dynamic viscosity. In our analysis, we approximated the value $k = 1.5\ \mathrm{s}^{-1}$, which is on the order of magnitude of the rotational diffusion coefficient $D_{rot} = k_B T/8\pi\eta R^3$. This result lead to best fit of the experimental data in the non-linear least square sense. We further examined the impact of this parameter on the final fitted parameter ${E_{\mathrm{bs}}}^0$ and found that its impact was less than 10% of the final value for the interval 0.75 s^{-1} and 3 s^{-1}.

Inserting equation 6.4 into equation 6.3 and integrating, we finally obtain

$$P_S(t) = \exp\left\{-k_0 \exp\left(-{E_{\mathrm{bs}}}^0\right)\frac{\Delta t}{{E_{\mathrm{bs}}}^0 c_p}\left[\exp\left({E_{\mathrm{bs}}}^0 c_p \frac{t}{\Delta t}\right) - 1\right]\right\} \qquad (6.6)$$

The only unknown parameter in equation 6.6 is the depth of the potential well at the start of the experiment ${E_{\mathrm{bs}}}^0$, which we obtain by fitting the experimental data using the maximum likelihood estimation, as shown in Fig. 6.3. We collected over 100 events of both up and down transitions for two ramp lengths – 60 s and 120 s, yielding a final fit of ${E_{\mathrm{b1}}}^0 = 7.2\ \mathrm{k_B T}$ and ${E_{\mathrm{b2}}}^0 = 4.1\ \mathrm{k_B T}$, showing a significant discrepancy between the "Down" and the "Up" states.

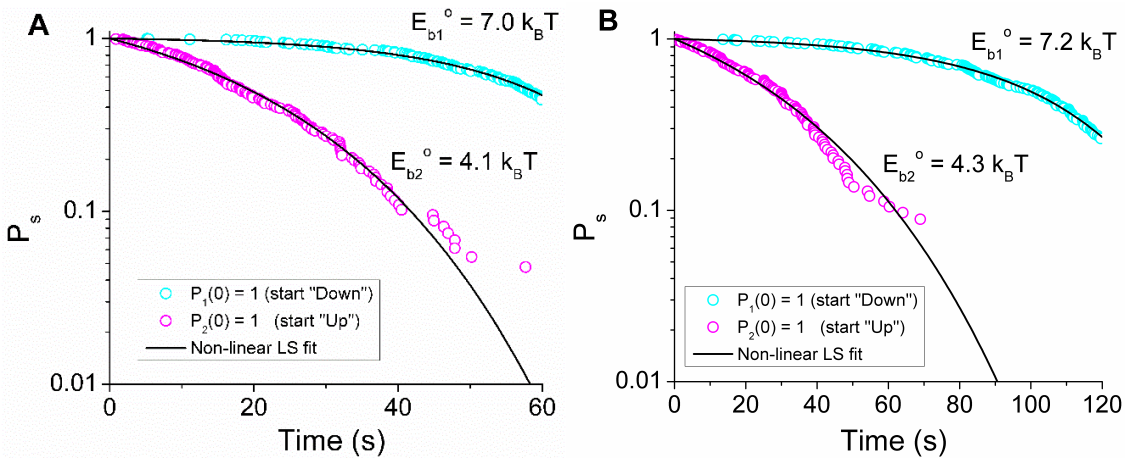

Figure 6.3. Initial state probabilities for laser power ramp experiment from 20 mW to 10 mW over (A) 60 s and (B) 120 s. The initial "Down" state (cyan circles) was significantly more stable compared to initial "Up" state (magenta circles), corresponding to almost twice as deep potential well at the bottom of the large bead compared to the top of the large bead.

From the results of the experiments, it is apparent that the "Down" state (Fig. 6.3, blue circles) is much more stable, compared to the "Up" state. With known ratio of the two potential wells, we can now revisit the results of Chapter 3, where we calculated this ratio as a function of the equilibrium position z_{eq} (Fig. 3.7 B). Comparing our experimental result to the values calculated using the Debye-type integral representation for the experimental parameters (λ = 806 nm, beam waist width w_0 = 411 nm, large bead radius r_l = 600 nm, small bead radius a = 100 nm, refractive index of the small bead n_2 = 1.57), we estimate the equilibrium position to be approximately 164 nm. Because the fits provide not only the ratio but also absolute value of the ground state energies, we can also evaluate the trapping beam power, which corresponds to ~ 3.45 mW. This is roughly 17% of the input beam. We therefore confirmed that the composite bead is indeed slightly behind the focus of the trapping beam at a distance of approximately 164 nm. This is relatively close to the geometrical optics limit $z_{eq}/a = 0.286$ [40], which predicts the distance of about 171.6 nm

Quantification of the Rotational Confinement

In the next experiment, we used the small bead tracking algorithm introduced in Chapter 5 to quantify the confinement of the rotational states for various laser powers. The measured values are compared to the simulation.

For laser powers ranging from 8 to 50 mW, the composite bead was recorded at 600 fps for more than 70 s, starting with the small bead in the "Up" position. In all of the recordings, the composite bead stayed in the "Up" state, with the exceptions for 8 mW, 10 mW, and 15 mW laser power. At these powers, the transitions happen at much shorter times than 70 s and we therefore analyzed only segments of the recordings in which the small bead was in the "Up" state for longer than 0.3 s.

The experiment is very sensitive to vertical alignment of the trapping beam and we therefore had to first post-process the data. The problem arises due to a slight tilt of the trapping beam due to imperfect vertical alignment of the trap, which causes the potential energy minimum to shift slightly away from the center of the bead from the objective viewpoint. To address this issue, we take advantage of the fact, that this very slight tilt can be also observed from the 3D positions of the composite bead (Fig. 6.4A). We therefore calculated the principal moment of inertia of the 3D bead positions and project it onto the XY plane to get the direction in which the potential energy minimum (or the small bead positions) were displaced (Fig. 6.4B). We then find the center of the small bead position distribution fitting a Gaussian to the probability density along this direction using the MLE. In the last step we calculate the radial distance of all small bead positions from the newly found center.

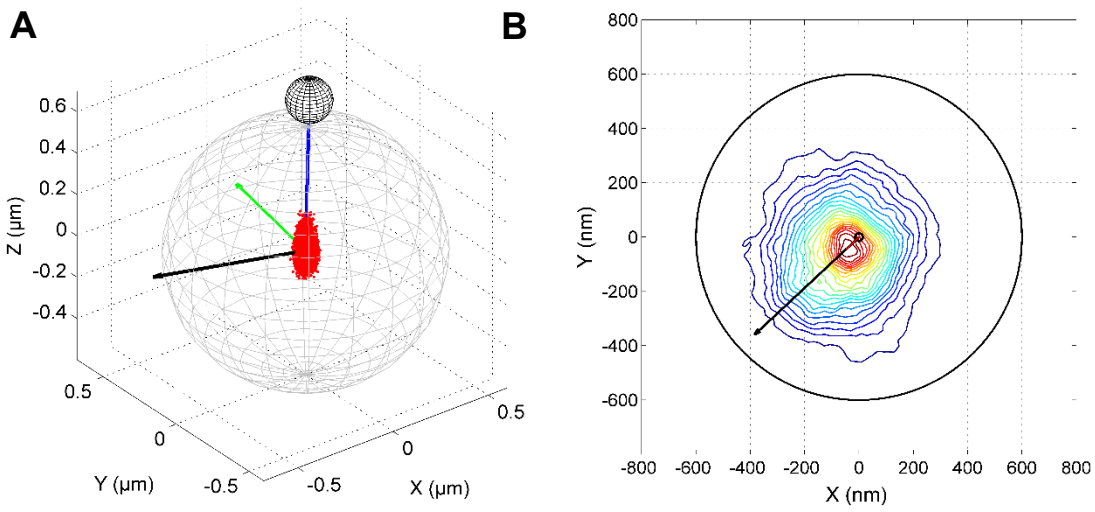

Figure 6.4. Post-processing of small bead tracking data. (A) From the 3D positions of the large bead (red), we find the moment of inertia axes (black, green and blue arrows). All elements drawn to scale. (B) Density of small bead positions, detected by the small bead tracking algorithm. The projection of the vertical moment of inertia onto the XY plane (black arrow) determines the direction of the displacement of the small bead position distributions. The new center of distribution is found by fitting a Gaussian to the probability density along the projection using MLE (not shown).

The standard deviation of the radial distribution corresponds to how tightly the trapping beam confines the rotational motion of the composite bead. We therefore use the MLE method to fit a zero-centered half-Gaussian and retrieve the variance of the small bead positions. In Fig. 6.5 are shown the MLE fits to the radial positions, weighted by the corresponding annulus surface.

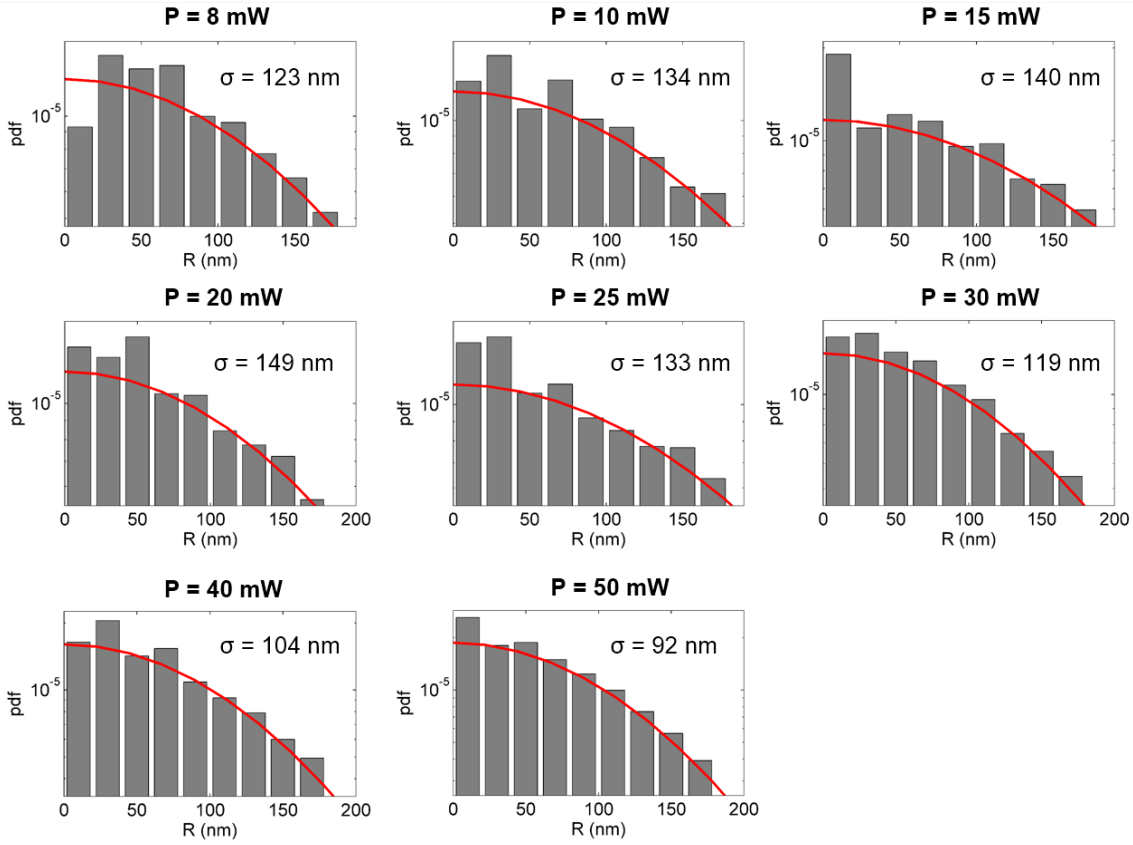

Figure 6.5. Mapping of the rotational potential using small bead tracking algorithm. The radial distances from the computed center of the distribution (see Fig. 6.9) are fitted using zero-centered half-Gaussian using the MLE. While no clear trend is apparent for the low powers, a significant narrowing of the distribution can be seen for the higher power.

The same data is plotted in Fig. 6.6, this time as an inverse variance of the small bead distributions as a function of the beam power. From the trend of the data, we see that values for 20 mW and up fall on a straight line, while the data for 8 mW, 10 mW and 15 mW are scattered. As already mentioned, the composite bead undergoes quite frequent transitions between the "Up" and "Down" states for powers lower than 20 mW. Although we developed an algorithm to detect "Up" and "Down" states of the bead, the detection is not perfect, especially for very short-lived states. Due to this reason, the data very likely includes some positions in the "Down" states for which our tracking algorithm does not work. Because of this, we decide to exclude these data points from the analysis. Since we

expect the variance to be infinite at zero power (uniform distribution within the probed region), we fit the data with a straight line going through origin (Fig. 6.6, black dashed line), with resulting slope of 2.297×10^{-6} $nm^{-2}mW^{-1}$ with 95% confidence interval of 2.253×10^{-6} to 2.341×10^{-6} $nm^{-2}mW^{-1}$.

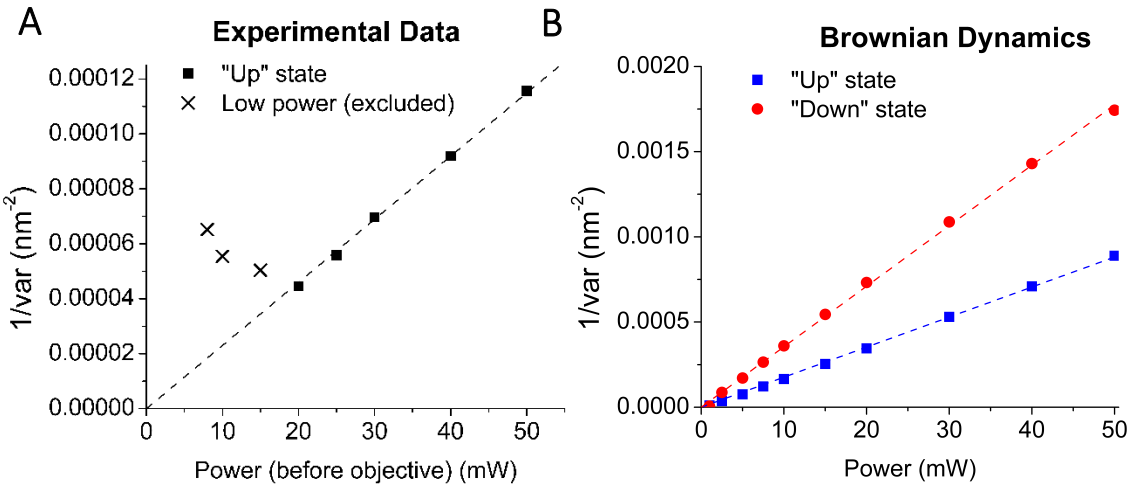

Figure 6.6. Inverse variance of small bead positions as a function of the beam power. The experimental data (A) show a very good linear fit for laser powers 20 mW and higher. At the low powers, the composite bead quickly transitions between the "Up" and "Down" states which results in inaccurate data (see text for more details) and we therefore exclude these data points from the analysis. The dashed line shows a linear fit going through the origin. The simulation data (B) allows us to probe both "Up" and "Down" states even for very low trapping laser powers. The ratio of the slopes from experimental data and the Brownian dynamics simulation estimates that the laser power at the focal plane is approximately 17% of the power before the objective.

To compare the result with our simulation, we repeat the same procedure with the data obtained by Brownian dynamics simulation performed with parameters matching that of the experiment (we use the equilibrium position established by the power ramp experiment, z_{eq} = 164 nm). The results shown in Fig. 6.6B confirm the linearly increasing inverse variance, even for very low powers. The linear fit of the "Up" state showed higher variance compared to the "Down" state as expected from theory. The linear fit of

the “Up” state variance (Fig. 6.6B, blue dashed line) yielded slope of 1.763×10^{-5} $nm^{-2}mW^{-1}$ with 95% confidence interval of 1.76×10^{-5} to 1.79×10^{-5} $nm^{-2}mW^{-1}$.

The only difference between the two plots is that the x axis for the experimental data represents the laser beam power before entering the objective, while the simulation data is dependent on the power of the beam at the focal plane. The ratio of the two slopes therefore allows us to get an estimate of the power passing through the objective and provide a check of the value obtained from the power ramp experiment. The resulting ratio 0.13 corresponds to 13% of the laser beam power being transmitted to the focal plane and is fairly close to the 17% estimated by the power ramp experiment.
Both of the power estimates show a significant power decrease, which cannot be explained only by transmittance of the objective, which is ~ 70% for wavelength $\lambda = 806$ nm, according to the data from manufacturer. This experimental evidence supports the assumptions that we overfill the objective and justifies our beam waist estimate $w_0 = 411$ nm.

CHAPTER 7

SUMMARY AND DISCUSSION

This last chapter provides a brief summary of the main results of this thesis, which is followed by discussion of the relevance of our findings for biological experiments. At the end we conclude by envisioning possible future directions of the research and possible applications of the composite beads.

In this thesis, we combined theoretical, computational and experimental approach to investigate the dynamics of the composite beads, which were initially intended as a model system for study of interaction between mesoscopic biological agents (such as viral particles) with cell surfaces. The project's focus shifted on the dynamics of composite beads when we first theoretically predicted and subsequently experimentally confirmed an unexpected rotational symmetry breaking caused by attachment of a small diameter sphere to the trapped microsphere.

We first examined the underlying physical principles using the Debye-type integral representation and Rayleigh scattering, which predicted a bistable potential energy landscape for the rotational states of the composite bead. The predicated potential energy wells were on the order of ~ 1 k_BT per mW of the trapping laser power at the focal plane. To obtain the beam waist parameter, we used a numerical integration of the Debye-type integral under the assumption of overfilling the microscope objective (this assumption was later confirmed by the experimental results). We also predicted a second, top-down symmetry breaking due to the shift in equilibrium position of the composite bead, resulting in unequal depths of the two potential wells. Because it is very difficult to measure or theoretically estimate the equilibrium shift, we investigated the symmetry breaking as a function of the equilibrium shift. In the whole process, we quantitatively compared the exact solution to the wave equation – the Debye-type integral – to a

solution to the paraxial wave equation – the Gaussian beam. Surprisingly, the Gaussian beam showed a relatively good degree of accuracy even for the highly convergent beam in our experimental setup.

In the second step, we designed a Brownian dynamics simulation to probe the composite bead dynamics under varying conditions. The simulation confirmed the predicted rotational symmetry breaking as a result of increasing laser power. Very low trapping power of ~ 1 mW allowed almost free rotation of the composite bead. For beam powers under 5 mW, the confinement of the rotational states became much more pronounced, although we were still able to observe thermally activated transitions between the two states. For powers of 7.5 mW all transitions were abolished and the composite bead remained locked in one of the rotational states.

The experimental section of the thesis consisted of two major experiments: power ramp experiments and quantification of the rotational confinement. In the former, we took advantage of the thermally activated transitions under linearly decreasing laser power to quantify the depth of the two potential energy wells and their ratio. To analyze the data we used the Kramers' theory to estimate the kinetic rates for the transitions and the depths of the potential wells. The potential well depths showed the value of 4.2 k_BT for the "Up" state and 7.1 k_BT for the "Down" state at the beam power of 20 mW (power before the objective). We then used the ratio of the potential wells 0.59 to find the equilibrium shift of the trapped bead. The result z_{eq} = 164 nm is very close to the geometrical optics limit of 171.6 nm. In addition, we estimated the power at the focal plane to be ~ 3.45 mW, roughly 17% of the beam power before entering the objective.

The second experiment involved a development of a new image processing algorithm that allowed us to track the rotational states of the composite bead. Regretfully, the tracking was possible only for the "Up" state of the particle, as the small bead became virtually invisible in the "Down" state. We tracked the small bead positions for laser powers between 8 and 50 mW. Because of slight tilt of the laser beam caused by

imperfect alignment of the optical trap, we used the moment of inertia of the 3D positions of the large bead to find a new center of the small bead position distributions. We then quantified the small bead position distributions in the central region of the image using maximum-likelihood estimate to fit a Gaussian distribution. The resulting fits showed an increasing confinement of the rotational states of the composite bead. When we plotted the inverse variance of the small bead distributions as a function of the laser power, we saw a very good linear fit for increasing laser power. Finally, we used the same procedure to quantify the simulation data and compare the two results. Because the experimental data is defined as a function of the beam power before entering the objective, while the simulation is based on the power at the focal plane, we could estimate the fraction of the power at the focal plane. The final fit yielded a value of ~ 13%, which is in fairly good agreement with the power ramp experiment.

From the perspective of biological experiments, the results of this thesis provide an interesting input. When working with mesoscopic biological agents attached to a microsphere, the optical trap will orient the composite bead to one of the low energy states. If the experimenter intends to change the orientation of the trapped microsphere, the trapping power must be sufficiently lowered, to allow for the thermal excitations to overcome the rotational confinement. The locking of orientation along the trapping beam axis is very advantageous to the vertical beam setup in which the trapped microsphere interacts with cell surface directly below. In a horizontal optical tweezers, more caution must be applied.

Perhaps more interestingly, the composite beads provide a very simple system for studying of thermally activated transition phenomena and the energetics of spontaneous symmetry breaking. The precise and simple control of the energy landscape through the laser power and the developed algorithms, which provide a fairly robust online monitoring of the rotational state of the composite bead in addition to precise offline analysis may provide excellent tool to study thermodynamical phenomena such as the

information to energy conversion. Although this thesis deals with a very simple composite bead with one small and one large bead attached, the results may be applied to systems with more than one small bead attached, which may be a source of even more interesting dynamics.

APPENDIX A

SPRING CONSTANT CALCULATION BASED ON ELECTROSTATIC APPROXIMATION

This appendix shows derivation of the formulas used to obtain spring constants of the optical trap for the large trapped sphere based on the beam waist and power. The formulations are based on the Electrostatic Approximation (ESA) and Gaussian beams introduced in Chapter 2 and agree with the formula (2.5) in the Rayleigh limit $a \ll \lambda$.

As discussed in previous chapter, a Gaussian beam shape can be completely described by only two parameters: the wavelength in given media λ and the beam waist w_0. In practice, only the information about the beam waist is unknown since the wavelength of the beam is controlled by the experimenter. In our case, we estimate the beam waist by numerical integration of the Debye-type integral representation and matching the result to a Gaussian.

Assuming a trapped sphere of radius a, we first transform the sphere surface positions (r_s, z_s) from cylindrical coordinates referenced to the beam center to spherical coordinates referenced to the trapped sphere center (r_a, z_a) (Fig. A.1):

$$\begin{aligned} {r_s}^2 &= a^2 \sin^2\theta \sin^2\phi + (r_a + a\sin\theta\cos\phi)^2 \\ &= a^2 \sin^2\theta + {r_a}^2 + 2r_a a \sin\theta\cos\phi \end{aligned} \tag{A.1}$$

$${z_s}^2 = (z_a + a\cos\theta)^2 \tag{A.2}$$

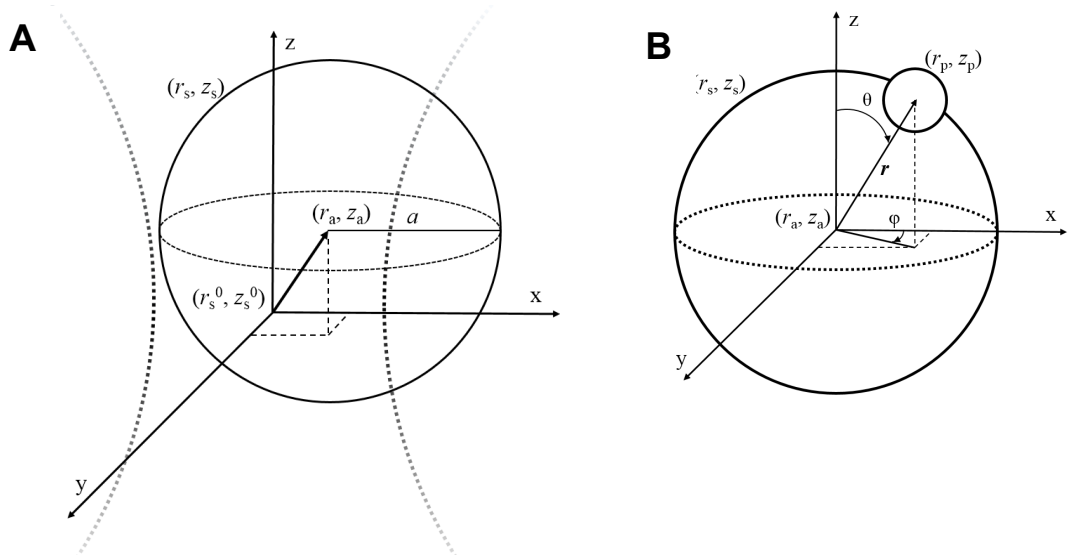

Figure A.1. Coordinate transform from cylindrical coordinates to spherical coordinates. The large bead surface position (r_s, z_s) are transformed from cylindrical coordinates referenced to the Gaussian beam center (r_s^0, z_s^0) (A) to spherical coordinates with respect to the large bead center (r_a, z_a), where a is the large bead radius, φ is the azimuthal angle and θ is the polar angle (B).

Inserting the Gaussian beam intensity (Eq. 2.8) into the result of the ESA (Eq. 2.16) and using substitution $\mu = \cos(\theta)$, we obtain the relations for force in the lateral and axial directions:

$$F_r \simeq \left(\frac{\alpha n_2 a^2}{2c}\right)\int_0^{2\pi} d\phi \cos\phi \int_{-1}^{1}\sqrt{1-\mu^2}\cdot I(r_s, z_s)d\mu \qquad (A.3)$$

$$F_z \simeq \left(\frac{\alpha n_2 a^2}{2c}\right)\int_0^{2\pi} d\phi \int_{-1}^{1}\mu\cdot I(r_s, z_s)d\mu \qquad (A.4)$$

Since we assume only small oscillations of the large bead around equilibrium ($r_a, z_a \ll a$), we can use the Taylor expansion of the Gaussian beam intensity I(r_s, z_s) for small displacements of the large bead relative to the beam center (r_s^0, z_s^0).

$$I(r_s, z_s) = I({r_s}^0, {z_s}^0) + \left\{\frac{\partial I}{\partial({r_s}^2)}\frac{\partial({r_s}^2)}{\partial r_s}\right\}_{{r_s}^0,{z_s}^0} r_a + \frac{1}{2}\left\{\frac{\partial^2 I}{\partial({r_s}^2)^2}\left[\frac{\partial({r_s}^2)}{\partial r_a}\right]^2 + \frac{\partial I}{\partial({r_s}^2)}\frac{\partial^2({r_s}^2)}{\partial {r_a}^2}\right\}_{{r_s}^0,{z_s}^0} {r_a}^2 + \cdots \quad \text{(A.5)}$$

$$I(r_s, z_s) = I({r_s}^0, {z_s}^0) + \left\{\frac{\partial I}{\partial({z_s}^2)}\frac{\partial({z_s}^2)}{\partial z_s}\right\}_{{r_s}^0,{z_s}^0} z_a + \frac{1}{2}\left\{\frac{\partial^2 I}{\partial({z_s}^2)^2}\left[\frac{\partial({z_s}^2)}{\partial z_a}\right]^2 + \frac{\partial I}{\partial({z_s}^2)}\frac{\partial^2({z_s}^2)}{\partial {z_a}^2}\right\}_{{r_s}^0,{z_s}^0} {z_a}^2 + \cdots \quad \text{(A.6)}$$

The force on the large bead can then be calculated by inserting the results of equations A.5 and A.6 into equations A.3 and A.4, respectively. In the last step, we take the derivative of the resulting formula, which is equal to the spring constants of the trap

$$k_{\mathrm{r}} \cong \frac{2\alpha n_2 \pi a^3 I_0}{{w_0}^2 c}\int_{-1}^{1}(1-\mu^2)\left(\frac{1}{1+\frac{\tilde{\alpha}^2\mu^2}{\pi^2 {w_0}^4}}\right)^2 \exp\left\{\frac{-2\tilde{\alpha}^2(1-\mu^2)}{\left(\widetilde{w}_0{}^2 + \frac{\tilde{\alpha}^2\mu^2}{\pi^2 {w_0}^2}\right)}\right\}\mathrm{d}\mu \quad \text{(A.7)}$$

$$k_z \cong \frac{2\alpha n_2 \pi a^3 I_0}{{w_0}^2 c}\left(\frac{\lambda}{\pi \widetilde{w}_0}\right)^2 \int_{-1}^{1} \mu^2 \left(\frac{1}{1+\frac{\tilde{a}^2\mu^2}{\pi^2 {w_0}^4}}\right)^2 \exp\left\{\frac{-2\tilde{a}^2(1-\mu^2)}{\left({\widetilde{w}_0}^2+\frac{\tilde{a}^2\mu^2}{\pi^2 {w_0}^2}\right)}\right\} \cdot \left(1-\frac{2\tilde{a}^2(1-\mu^2)}{\left({\widetilde{w}_0}^2+\frac{\tilde{a}^2\mu^2}{\pi^2 {w_0}^2}\right)}\right) \mathrm{d}\mu \tag{A.8}$$

where $\tilde{a} \equiv a/\lambda$ is the normalized bead radius and $\widetilde{w}_0 \equiv w_0/\lambda$ is the normalized Gaussian beam waist.

As a verification of the ESA, we calculate the forces on the small bead in optical trap and compare them to the formulas for Rayleigh limit. First, we expand the intensity for surface positions with respect to the small particle diameter a_p:

$$I(r_p, z_p) = I({r_p}^0, {z_s}^0) + \left\{\frac{\partial I}{\partial({r_s}^2)}\frac{\partial({r_s}^2)}{\partial a}\right\}_{a\to 0} a_p + \cdots \tag{A.9}$$

$$I(r_p, z_p) = I({r_p}^0, {z_s}^0) + \left\{\frac{\partial I}{\partial({z_s}^2)}\frac{\partial({z_s}^2)}{\partial a}\right\}_{a\to 0} a_p + \cdots \tag{A.10}$$

After taking the appropriate derivatives of the Gaussian beam intensity (Eq. 2.8) and inserting once again into Eq. 2.16, one obtains:

$$F_{\mathrm{r}} \cong \left(\frac{\alpha n_2 {a_p}^3}{c}\right)\left(\frac{-2r_p \mathrm{I}(r_{\mathrm{p}}, z_{\mathrm{p}})}{w^2}\right)\int_0^{2\pi}\cos^2\phi\,\mathrm{d}\phi\int_{-1}^{1}(1-\mu^2)\mathrm{d}\mu$$
$$\cong -2\left(\frac{\alpha n_2 v_p}{c}\right)\frac{r_{\mathrm{p}}\mathrm{I}(r_{\mathrm{p}}, z_{\mathrm{p}})}{w^2} \tag{A.11}$$

$$F_{\mathrm{z}} \cong \left(\frac{\alpha n_2 {a_p}^3}{c}\right)\left[-\left(\frac{w_0}{z_{\mathrm{p}}}\right)^2\left(1-\frac{2{r_{\mathrm{p}}}^2}{w^2}\right)\frac{\mathrm{I}(r_{\mathrm{p}}, z_{\mathrm{p}})}{w^2}\right]2\pi\int_{-1}^{1}\mu^2\mathrm{d}\mu$$
$$\cong -\left(\frac{\alpha n_2 v_p}{c}\right)\left(\frac{w_0}{z_{\mathrm{p}}}\right)^2\left(1-\frac{2{r_{\mathrm{p}}}^2}{w^2}\right)\frac{z_{\mathrm{p}}\mathrm{I}(r_{\mathrm{p}}, z_{\mathrm{p}})}{w^2} \tag{A.12}$$

where $\mathrm{I}(r_{\mathrm{p}}, z_{\mathrm{p}})$ is the Gaussian beam intensity. Here, we have employed the assumption that the intensity is constant over the integration volume due to the small size of the bead. We note both equations A.11 and A.12 are equal to equation (16) in Harada & Asakura [22], after derivation and substitution

$$\alpha = m^2 - 1 \cong \frac{3(m^2-1)}{(m^2+2)} \tag{A.13}$$

Eq. (A.13) is one of the assumptions of the electrostatic approximation that the trapped particle is only slightly polarizable.

APPENDIX B

SEPARATION OF TIMESCALES FOR TRANSLATIONAL AND ROTATIONAL MOTION OF THE COMPOSITE BEADS

In this appendix, we show by few simple calculations that the time scales of translational and rotational motion are separated by at least two orders of magnitude. For translational motion, the timescale is defined as

$$\tau_T = \frac{\gamma}{\kappa} = \frac{k_\mathrm{B}\mathrm{T}}{\kappa \cdot D} \tag{B.1}$$

where γ is the friction coefficient, κ is the spring constant and D is the diffusion coefficient. For translational motion, the timescale is simply

$$\tau_R = \frac{\gamma_R}{k_\mathrm{B}\mathrm{T}} = \frac{1}{D_R} \tag{B.2}$$

where D_R is the rotational diffusion. The ratio of the equations (B.1) and (B.2), using the Stokes law $\gamma = 6\pi\eta r$ and $\gamma_R = 8\pi\eta r^3$ for drag coefficients, is

$$\frac{\tau_T}{\tau_R} = \frac{6\pi\eta r/\kappa}{8\pi\eta r^3/k_\mathrm{B}\mathrm{T}} = \frac{4}{3} \cdot \frac{k_\mathrm{B}\mathrm{T}}{\kappa} \cdot \frac{1}{r^2} \tag{B.3}$$

Even for extremely low spring constant ($\kappa = 0.001$ pN/nm), the ratio $k_\mathrm{B}\mathrm{T}/\kappa$ is on the order of 10^3 nm^2, whereas the bead radius squared is $\sim 10^5$ nm^2 and therefore we can assume sufficient separation between the translational and rotational time scale.

REFERENCES

1. Neuman, K. and S. Block, *Optical trapping.* The Review of scientific instruments, 2004. **75**(9): p. 2787-2809.
2. Moffitt, J.R., et al., *Recent advances in optical tweezers*, in *Annual Review of Biochemistry*. 2008, Annual Reviews: Palo Alto. p. 205-228.
3. Guck, J., et al., *The optical stretcher: a novel laser tool to micromanipulate cells.* Biophysical Journal, 2001. **81**(2): p. 767-784.
4. Ashkin, A. and J. Dziedzic, *Optical trapping and manipulation of viruses and bacteria.* Science, 1987. **235**(4795): p. 1517-1520.
5. McCann, L.I., M. Dykman, and B. Golding, *Thermally activated transitions in a bistable three-dimensional optical trap.* Nature, 1999. **402**(6763): p. 785-787.
6. Simon, A. and A. Libchaber, *Escape and synchronization of a Brownian particle.* Physical review letters, 1992. **68**(23): p. 3375-3378.
7. Grier, D.G., *Optical tweezers in colloid and interface science.* Current opinion in colloid & interface science, 1997. **2**(3): p. 264-270.
8. Roldan, E., et al., *Universal features in the energetics of symmetry breaking.* Nature Physics, 2014. **10**: p. 457-461.
9. Bérut, A., et al., *Experimental verification of Landauer's principle linking information and thermodynamics.* Nature, 2012. **483**(7388): p. 187-189.
10. Shoichi, T., et al., *Experimental demonstration of information-to-energy conversion and validation of the generalized Jarzynski equality.* Nature Physics, 2010. **6**: p. 988-992.
11. Grier, D.G., *A revolution in optical manipulation.* Nature, 2003. **424**(6950): p. 810-816.
12. Kepler, J., *De Cometis.* Libelli tres. Mylius: Augustae Vindelicorum. **1619**.

13. Maxwell, J.C., *A dynamical theory of the electromagnetic field.* Philosophical Transactions of the Royal Society of London, 1865. **155**: p. 459-512.

14. Ashkin, A., *Acceleration and trapping of particles by radiation pressure.* Physical review letters, 1970. **24**(4): p. 156-159.

15. Ashkin, A., *Forces of a single-beam gradient laser trap on a dielectric sphere in the ray optics regime.* Biophysical journal, 1992. **61**(2): p. 569-582.

16. Svoboda, K. and S. Block, *Biological applications of optical forces.* Annual review of biophysics and biomolecular structure, 1994. **23**: p. 247-285.

17. Ashkin, A., et al., *Observation of a Single-Beam Gradient Force Optical Trap for Dielectric Particles.* Optics Letters, 1986. **11**(5): p. 288-290.

18. Ashkin, A., *Forces of a single-beam gradient laser trap on a dielectric sphere in the ray optics regime.* Methods in cell biology, 1998. **55**: p. 1-27.

19. Ashkin, A., J. Dziedzic, and T. Yamane, *Optical trapping and manipulation of single cells using infrared laser beams.* Nature, 1987. **330**(6150): p. 769-771.

20. Stratton, J.A., *Electromagnetic theory*. 1941: McGraw-Hill book company, inc.

21. Kerker, M., *The scattering of light, and other electromagnetic radiation*. 1969: Academic Press.

22. Harada, Y. and T. Asakura, *Radiation forces on a dielectric sphere in the Rayleigh scattering regime.* Optics Communications, 1996. **124**(5): p. 529-541.

23. Lorenz, L., *Upon the light reflected and refracted by a transparent sphere.* Vidensk. Selsk. Shrifter, 1890. **6**: p. 1-62.

24. Mie, G., *Contributions to the optics of turbid media, particularly of colloidal metal solutions.* Contributions to the optics of turbid media, particularly of colloidal metal solutions Transl. into ENGLISH from Ann. Phys.(Leipzig), v. 25, no. 3, 1908 p 377-445, 1976. **1**: p. 377-445.

25. Laven, P., *Simulation of rainbows, coronas, and glories by use of Mie theory.* Applied optics, 2003. **42**(3): p. 436-444.

26. van de Hulst, H., *Light Scattering by Small Particles.* Light Scattering by Small Particles, New York: John Wiley & Sons, 1957, 1957. **1**.

27. Kogelnik, H. and T. Li, *Laser beams and resonators.* Applied optics, 1966. **5**(10): p. 1550-1567.

28. Richards, B. and E. Wolf, *Electromagnetic diffraction in optical systems. II. Structure of the image field in an aplanatic system.* Proceedings of the Royal Society of London. Series A. Mathematical and Physical Sciences, 1959. **253**(1274): p. 358-379.

29. Siegman, A.E., *Lasers University Science Books.* Mill Valley, CA, 1986. **37**.

30. Gouesbet, G., G. Gréhan, and B. Maheu, *Scattering of a Gaussian beam by a Mie scatter center using a Bromwich formalism.* Journal of optics, 1985. **16**(2): p. 83.

31. Gouesbet, G., B. Maheu, and G. Grehan, *Light scattering from a sphere arbitrarily located in a Gaussian beam, using a Bromwich formulation.* JOSA A, 1988. **5**(9): p. 1427-1443.

32. Davis, L., *Theory of electromagnetic beams.* Physical Review A, 1979. **19**(3): p. 1177.

33. Barton, J. and D. Alexander, *Fifth-order corrected electromagnetic field components for a fundamental Gaussian beam.* Journal of Applied Physics, 1989. **66**(7): p. 2800-2802.

34. Gouesbet, G., J.A. Lock, and G. Gréhan, *Partial-wave representations of laser beams for use in light-scattering calculations.* Applied optics, 1995. **34**(12): p. 2133-2143.

35. Gouesbet, G. and G. Gréhan, *Generalized Lorenz-Mie Theories*. 2011: Springer.

36. Nieminen, T., H. Rubinsztein-Dunlop, and N. Heckenberg, *Multipole expansion of strongly focussed laser beams.* Journal of Quantitative Spectroscopy and Radiative Transfer, 2003. **79**: p. 1005-1017.

37. Rohrbach, A. and E. Stelzer, *Optical trapping of dielectric particles in arbitrary fields.* Journal of the Optical Society of America. A, Optics, image science, and vision, 2001. **18**(4): p. 839-853.

38. Rohrbach, A., *Stiffness of optical traps: quantitative agreement between experiment and electromagnetic theory.* Physical review letters, 2005. **95**(16): p. 168102.

39. Neto, P. and H. Nussenzveig, *Theory of optical tweezers.* Europhysics Letters (epl), 2000. **50**(5): p. 702.

40. Mazolli, A., P. Neto, and H. Nussenzveig, *Theory of trapping forces in optical tweezers.* Proceedings of The Royal Society A: Mathematical, Physical and Engineering Sciences, 2003.

41. Viana, N., et al., *Towards absolute calibration of optical tweezers.* Physical review. E, Statistical, nonlinear, and soft matter physics, 2007. **75**(2 Pt 1): p. 21914.

42. Mahamdeh, M., C. Campos, and E. Schäffer, *Under-filling trapping objectives optimizes the use of the available laser power in optical tweezers.* Optics express, 2011. **19**(12): p. 11759-11768.

43. Tlusty, T., A. Meller, and R. Bar-Ziv, *Optical Gradient Forces of Strongly Localized Fields.* Physical Review Letters, 1998.

44. Zemánek, P., A. Jonáš, and M. Liška, *Simplified description of optical forces acting on a nanoparticle in the Gaussian standing wave.* JOSA A, 2002. **19**(5): p. 1025-1034.

45. Rossky, P., J. Doll, and H. Friedman, *Brownian dynamics as smart Monte Carlo simulation.* The Journal of Chemical Physics, 1978. **69**(10): p. 4628-4633.

46. Doi, M., *The theory of polymer dynamics*. Vol. 73. 1988: Oxford University Press.

47. Lax, M., *Fluctuations from the nonequilibrium steady state.* Reviews of modern physics, 1960. **32**(1): p. 25.

48. Kuznetsov, I. and E. Evans, *Brownian nanoimaging of interface dynamics and ligand-receptor binding at cell surfaces in 3-D.* Methods, 2013. **60**(2): p. 214-224.

49. Heinrich, V., et al., *Imaging biomolecular interactions by fast three-dimensional tracking of laser-confined carrier particles.* Langmuir, 2008. **24**(4): p. 1194-1203.

50. Wong, W.P. and K. Halvorsen, *The effect of integration time on fluctuation measurements: calibrating an optical trap in the presence of motion blur.* Optics express, 2006. **14**(25): p. 12517-12531.

51. Kramers, H.A., *Brownian motion in a field of force and the diffusion model of chemical reactions.* Physica, 1940. **7**(4): p. 284-304.